Unsteady Aerodynamic Optimization of Airfoil for Cycloidal Propellers Based on Surrogate Model

Jiwei Tang,* Yu Hu,† and Bifeng Song‡

Northwestern Polytechnical University, 710072 Xi'an, Shaanxi, People's Republic of China

and

Hui Yang§

Shanghai Aircraft Design and Research Institute, 200000 Shanghai, People's Republic of China

An effective unsteady aerodynamic-optimization method of airfoil for cycloidal propellers is developed. Firstly, the class-function/shape-function transformation parameterization method is adopted to describe the airfoil profile with different geometrical parameters. Secondly, the sample points in the design space are selected using the optimal Latin hypercube design methodology. Thirdly, the actual aerodynamic performance of cycloidal propellers is simulated by using the time-dependent incompressible Reynolds-averaged Navier–Stokes computational fluid dynamics method and the sliding-mesh technique, which are verified by validation cases on an oscillating NACA 0012 airfoil and the baseline cycloidal propeller. Then, to replace the time-consuming computational fluid dynamics solver, kriging surrogate models are established using the sample data. Finally, the genetic algorithm is adopted to determine the optimized airfoil in the design space based on the constructed kriging models. Optimization is conducted on a micro-four-bladed cycloidal propeller with the NACA 0015 airfoil, and the results show that the figure of merit of the cycloidal propeller is increased by 18.31% at the design rotation speed. Although the optimization is conducted only at the design rotation speed, an appreciable improvement of the figure of merit can be achieved for a wide range of rotation speeds.

Nomenclature

B_L	=	length of a blade span
b	=	number of blades
C_{LF}	=	blade lateral-force coefficient
C_{LT}	=	lateral-thrust coefficient
C_M	=	aerodynamic-torque coefficient
C_{mb}	=	blade aerodynamic-torque coefficient
C_N	=	blade normal-force coefficient
C_T	=	resultant thrust coefficient
C_t	=	blade tangent-force coefficient
C_{VF}	=	blade vertical-force coefficient
C_{VT}	=	vertical-thrust coefficient
c	=	chord length
D	=	diameter of the cycloidal propeller
F_L	=	instantaneous blade lateral force
F_N	=	instantaneous blade normal force
F_t	=	instantaneous blade tangent force
F_V	=	instantaneous blade vertical force
k	=	oscillating reduced frequency
M_b	=	instantaneous blade aerodynamic torque
R	=	radius of the cycloidal propeller
R_{LE}	=	leading-edge nose radius of an airfoil
s	=	projected area of the cycloidal propeller
T	=	time-averaged integral thrust of the cycloidal propeller during one revolution
T_L	=	instantaneous lateral-thrust component
T_V	=	instantaneous vertical-thrust component

T_x	=	time-averaged integral horizontal thrust of the cycloidal propeller during one revolution
T_z	=	time-averaged integral vertical thrust of the cycloidal propeller during one revolution
V_R	=	rotational velocity of the blade
α_{bot}	=	pitch angle of the blade at the bottom position of the orbit
α_p	=	instantaneous pitch angle of the blade
α_{top}	=	pitch angle of the blade at the top position of the orbit
α_ψ	=	pitch angle of the blade at azimuth ψ
β_t	=	boattail angle of an airfoil
ζ_{max}	=	maximal thickness of the baseline airfoil
ζ_t	=	trailing-edge thickness of an airfoil
ρ	=	air density
ψ	=	azimuth

I. Introduction

THE cycloidal propeller is a new concept of a rotary-wing system, whose blade span runs parallel to the rotation axis and perpendicular to the flight direction [1]. The blade pitch angle experiences a periodic variation over each revolution, which is induced by an eccentric ring through the push–pull linkages, such that the angles of attack (AOA) of the blade are positive at both the upper and lower cycles of the rotating orbit [2]. The orbit of a blade is a circle in hover vs a cycloid in forward flight. By changing the amplitude and phase angle of the eccentric ring relative to the rotation axis, the magnitude and direction of thrust can be varied instantaneously. Figure 1a shows a two-dimensional (2-D) sketch of a four-bladed cycloidal propeller.

As a new concept of lift or propulsion device other than the conventional propeller or rotor, the cycloidal propeller has some unique aerodynamic characteristics, which can be summarized as follows [1]. Firstly, unlike conventional propellers whose aerodynamic conditions vary from the blade root to the tip, the blade span of a cycloidal propeller is parallel to the rotation axis. Thus, the blade sections along the span operate at similar flow conditions, allowing for all spanwise blade sections to be optimized for operating at their peak aerodynamic efficiency [3]. Secondly, as the blade continuously oscillates and the pitching angle changes cyclically, the blade-stall onset is delayed and the corresponding unsteady dynamic lift can reach much higher values than the

*Ph.D., School of Aeronautics; tangjw1987@126.com.
†Associate Professor, School of Aeronautics; julius_hu@hotmail.com. Member AIAA.
‡Professor, School of Aeronautics; sbf@nwpu.edu.cn.
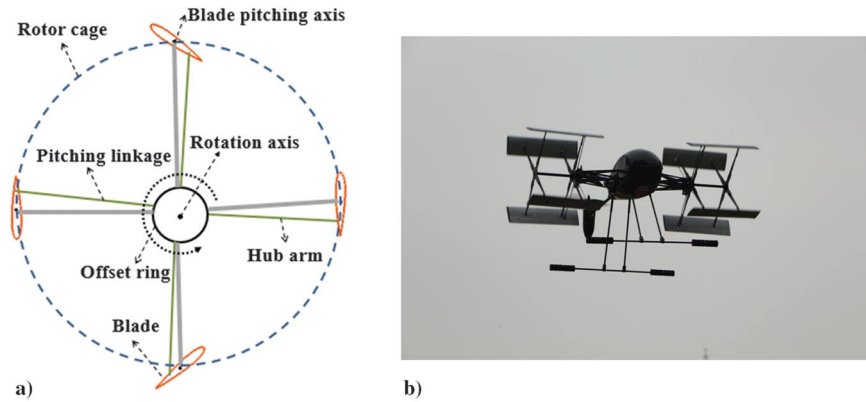§Engineer, General Configuration and Aerodynamics Department; ya_ben_cool@126.com.

Fig. 1   a) Construction of a four-bladed cycloidal propeller; b) a cyclocopter in flight.

maximum achievable static lift [4]. Thirdly, by changing the amplitude and phase angle of the offset ring, the magnitude and direction of the resultant thrust produced by a cycloidal propeller can be changed easily and instantly. This characteristic provides the cycloidal propeller with unique capabilities, such as vertical takeoff and landing (VTOL), sustained hovering, and forward flight [5]. In addition, according to the experiments and numerical simulations, the aerodynamic efficiency of a cycloidal propeller can be higher than that of the conventional propeller or helicopter rotor if properly designed [6]. Therefore, cycloidal propellers are readily pursued as an alternative for a variety of applications [7], such as VTOL vehicles, micro air vehicles (MAVs), and airships. Figure 1b shows a flight-capable twin cyclocopter developed in Northwestern Polytechnical University, which consists of a conventional microrotor and two four-bladed cyclorotors. The conventional microrotor is necessary to counteract the torque from the two cyclorotors, and is also used for pitch control.

Although the concept of cycloidal propeller has been studied since the 1920s to the 1940s [8,9], most studies have been conducted in the recent 20 years owing to the technological advancements in subjects of unsteady aerodynamics and flight-control strategy. To understand more about the fundamental aerodynamic characteristics of a cycloidal propeller, some studies have been done to investigate the effects of design parameters, such as blade number, pitching angles, and blade airfoil, on the overall aerodynamic performance and efficiency in hovering flight [10–18]. Among these parameters, the blade airfoil is one of the most commonly concerned parameters. On one hand, it is studied through the experimental method. For example, in [1], Benedict et al. tested the aerodynamic performance of cycloidal propellers with different blade-airfoil profiles, among which the thickest airfoil is NACA 0010. They found that the NACA 0010 blades produced the highest thrust at all tested pitching amplitudes, but the reverse NACA 0010 blades produced better power loadings at lower pitching amplitudes. After that, Jarugumilli et al. did some work on the aerodynamic-performance analysis and optimization of a MAV-scale cycloidal rotor through a series of parametric experimental studies [12]. The airfoil test cases showed that, among the three airfoil profiles (NACA 0006, NACA 0010, and NACA 0015), the NACA 0015 airfoil produced the best power loading, followed by the NACA 0010 airfoil and the NACA 0006 airfoil. Recently, Hu and Zhang [19] made some experiments and numerical simulations for cycloidal propellers with five airfoil profiles (flat plat, NACA 0006, NACA 0012, NACA 0015, and NACA 0018). The experimental results showed that the cycloidal propeller with the NACA 0015 airfoil achieved the highest figure of merit (FM); the numerical simulations showed that the maximum thickness and leading-edge radius of an airfoil significantly affected the flowfield and the aerodynamic performance of the cycloidal propeller.

Because of inadequate understanding about the unsteady aerodynamics of a cycloidal propeller, one of the most challenging tasks in the cycloidal-propeller design remains to increase its aerodynamic performance to a higher level by suitable selection of design parameters. The current way to select the airfoil is directly making the parametric studies just like the methods shown in [11,12,19]. However, without considering the interactive effects, only a few numbers of airfoils (usually less than 10) are studied to analyze the individual effects of thickness or camber of airfoil, and the airfoil selected by this method is usually just the best one among the tested airfoils. Therefore, if a detailed design is required, an optimization method to determine the best airfoil in a certain design space needs to be established. However, to the best of the authors' knowledge, few papers about the airfoil-optimization method for cycloidal propellers are available in the literature by far.

The aim of this study was to develop an effective airfoil-optimization method for cycloidal propellers based on the surrogate model. In this method, the maximum FM is used as the objective function, because a high FM is the basic requirement for the cycloidal propeller. The class/shape transformation (CST) parameterization method [20,21] is adopted to model the airfoil geometry in a simple but efficient way. The sample data in the design space are selected using the optimal Latin hypercube design (OLHD) methodology, which has not only the advantage of "full filling," but also can guarantee the symmetric distribution of sampling points in the whole design space. The actual aerodynamic solutions are generated by using the time-dependent incompressible Reynolds-averaged Navier–Stokes (RANS) computational fluid dynamics (CFD) method and sliding-mesh technique. And the surrogate models are established based on the kriging model to replace the time-consuming CFD solver. Besides, due to the fact that the unsteady aerodynamic-optimization problems are governed by nonlinear physics, genetic algorithm (GA) is used as the optimization methodology.

II.   Methodology

A.   CST Parameterization Method

The CST method is a powerful airfoil-parameterization approach, whose formulation is simple and robust [22]. The coupling of analytic shape-function with class-function geometric transformation technique provides the capability to represent a wide variety of 2-D and three-dimensional (3-D) shapes encompassing a very large design space with a relatively few parameters [20].

The general key design parameters for an airfoil with a circular leading-edge round-nose airfoil are shown in Fig. 2, in which c is the chord length, R_{LE} is the leading-edge radius, T_{max} is the maximum thickness, β_t is the airfoil boattail angle, and ΔZ_t is half of the trailing-edge thickness. The coordinates of the airfoil geometry can be defined in terms of the class function and shape function as follows:

$$\zeta(\psi) = C(\psi)S(\psi) + \psi\zeta_t \qquad (1)$$

in which $\zeta = z/c$, $\psi = x/c$; $\zeta_t = \Delta z_t/c$ represents the nondimensional thickness of the trailing edge. The class function $C(\psi)$ is used to define the general classes of geometries, which is defined by
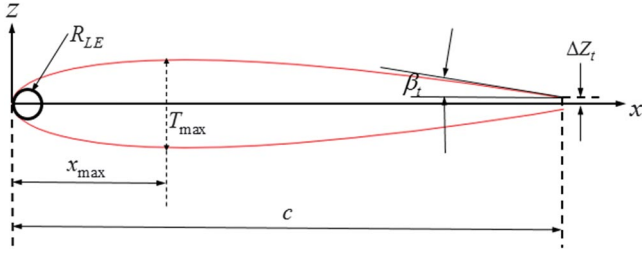
Fig. 2   General schematic of the geometric parameters for an airfoil.

$$C(\psi) = \psi^{N_1}(1 - \psi)^{N_2} \tag{2}$$

In Eq. (2), different combinations of N_1 and N_2 define different basic classes of geometric shapes [21]. For a NACA airfoil, $N_1 = 0.5$ and $N_2 = 1.0$.

The shape function $S(\psi)$ is derived from the basic geometry equation, which is defined by

$$S(\psi) = \frac{\zeta(\psi) - \psi\zeta_t}{C(\psi)} \tag{3}$$

Using Bernstein polynomials (BPs) of the unit shape function, the overall shape-function equation for the upper surface of the airfoil geometry is written as

$$S_u(\psi) = \sum_{i=0}^{N} A_{ui} \cdot S_i(\psi) \tag{4}$$

And the overall shape-function equation for the lower surface of the airfoil geometry is written as

$$S_l(\psi) = \sum_{i=0}^{N} A_{li} \cdot S_i(\psi) \tag{5}$$

in which

$$S_i(\psi) = \frac{N!}{i!(N-i)!}\psi^i(1 - \psi)^{N-i} \tag{6}$$

in which N represents the BP order (BPO), and i represents the sequence number of the order.

According to [21], the coefficients A_{u0} and A_{l0} are directly related with the upper and lower leading-edge radii, to satisfy the continuity in curvature of the leading-edge radius; A_{u0} needs to be equal to A_{l0}. Besides, the value of the shape function at $x/c = 0$ has a direct relationship with the airfoil leading-edge radius R_{LE}, which can be expressed as

$$S(0) = \sqrt{2 \cdot R_{LE}/c} \tag{7}$$

And the value of the shape function at $x/c = 1$ has a direct relationship with the airfoil boattail angle β_t and the trailing-edge thickness ζ_t, which can be written as

$$S(1) = \tan\beta_t + \zeta_t \tag{8}$$

According to the preceding analysis, once the unknown coefficients A_{ui} and A_{li} for the BP shape functions are determined by techniques, such as the least-squares fit method, the airfoil geometry can be parametrically defined.

Generally, with the increasing of the BPO, the precision of the CST method is higher. However, a higher BPO means more design variables are needed in the optimization process, and thus cause a large number of numerical simulations. Therefore, a suitable BPO is required to meet both the requirements of precision and
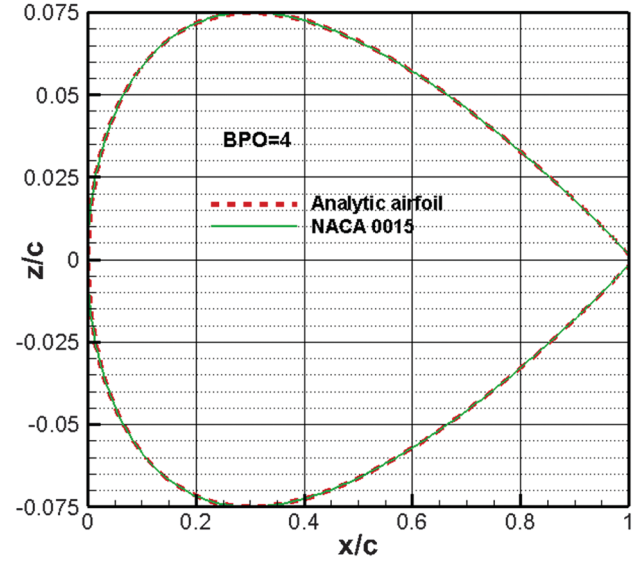

Fig. 3   Comparisons of the shape of actual airfoil and representative airfoil.

computational cost. In the present study, BPO = 4 is selected as the BPO, and hence nine design variables are optimized in the airfoil aerodynamic optimization.

The comparisons of the actual coordinates of the NACA 0015 symmetric airfoil and the analytic airfoil shape calculated by the CST method are shown in Fig. 3. Figure 4 shows the corresponding residual difference between the actual NACA 0015 airfoil geometry and the approximated airfoil. It can be seen from Fig. 3 that the approximated airfoil shape matches well with the actual airfoil. As shown in Fig. 4, the maximum residual difference is only about 2.8×10^{-4}, which is lower than the typical wind-tunnel-model tolerance [21].

B.   Establishment of a Surrogate Model

For the problem of unsteady aerodynamic optimization of an airfoil for cycloidal propellers, if direct optimization is adopted, it will be computationally intensive. Therefore, a surrogate model needs to be constructed to replace the actual CFD unsteady simulations in the optimization process. In this section, the surrogate model adopted is introduced, which is a basic model for the subsequent optimization process.
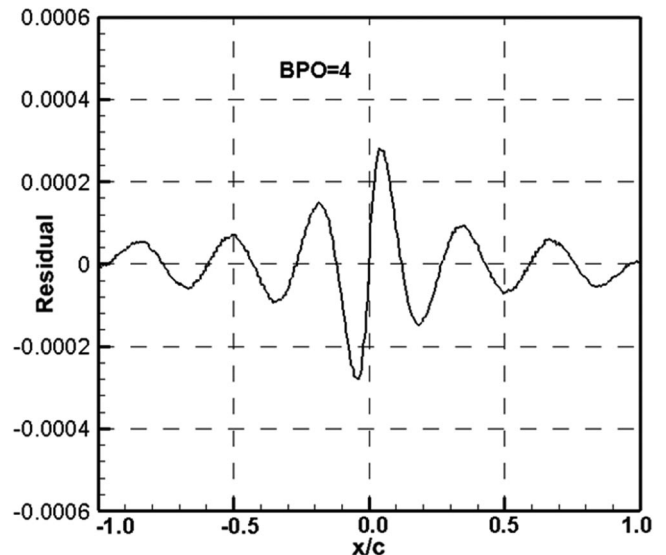

Fig. 4   Residual difference of geometry between the actual airfoil and the approximated airfoil.
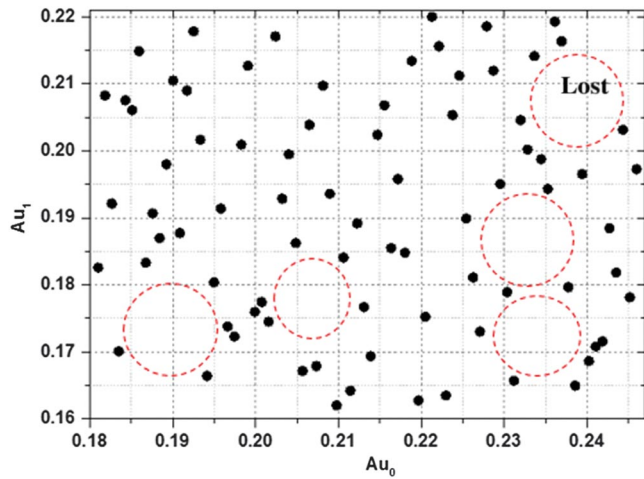
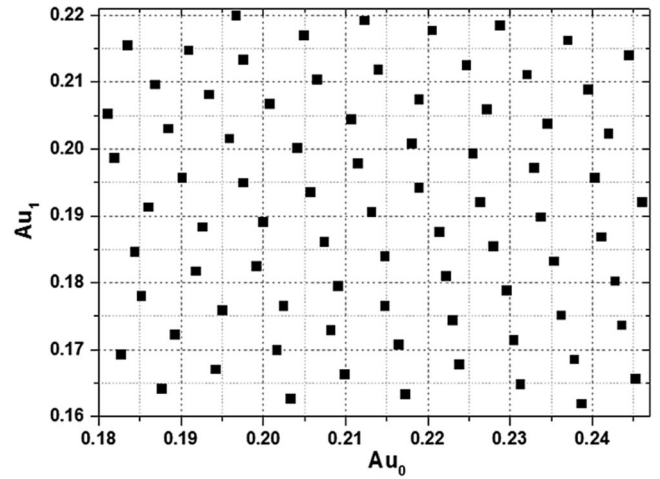**Fig. 5 Distribution of A_{u0} and A_{u1} calculated by the LHD method.**

Fig. 6 Distribution of A_{u0} and A_{u1} calculated by the OLHD method.

1. Design of Experiment

The use of the design-of-experiment (DOE) method [23] is required to generate the sampling points. The DOE approach is widely adopted to analyze a system with a small number of sampling points. It helps to acquire the whole information of the model in the design space with a significant reduction of computational cost. However, as different DOE methods have different sampling strategies, the choice of a DOE method may result in different sampling points in the same design space, which will greatly affect the precision of the surrogate model. The widely used DOE methods include full factorial design (FFD), parameter study (PS), orthogonal array (OA), central composite design (CCD), Latin hypercube design (LHD), OLHD, et al.

The LHD method was firstly proposed by McKay et al. [24], and it has been one of the most widely used DOE methods. Compared with the FFD, PS, OA, and CCD methods, the LHD can generate sampling points that better fill in the defined design space. In practice, however, the sampling strategy of the LHD has the property of randomness, which may lead to a nonsymmetric distribution of the sampling points, and hence some area in the design space could not be considered [25]. Meanwhile, with the increasing number of design factors, the lost area where no sampling points are present will increase. Figure 5 shows the 2-D design space of A_{u0} and A_{u1}, which are the first two polynomials defined in Eq. (4) for the NACA 0015 airfoil. As shown in Fig. 5, by using the strategy of the LHD, some design spaces are obviously lost, where are marked in the dashed circle.

The OLHD [25] is an improved LHD method. This approach provides a compromise between the good projective properties of the LHD and minimizing the integrated mean-square error [23] or maximizing the entropy [26]. Therefore, by using the OLHD, the whole design space can be fully filled with the symmetrical sampling points. Figure 6 shows the distribution of A_{u0} and A_{u1}, whose design spaces are equal to that of Fig. 5. As shown in Fig. 6, the sampling points show good capability of filling and symmetry distribution. According to the preceding analysis, the experiment design of the BPs is dealt with the OLHD method in the present study.

Figure 7 shows a schematic of the design space for aerodynamic optimization. The solid line represents the baseline airfoil (NACA 0015). The short dashed line and the long dashed line represent the lower bound (thin airfoil) and the upper bound (thick airfoil) of the design space, respectively.

2. Surrogate Model

Surrogate modeling can be regarded as an approximated technique that makes use of the sampling data obtained by the DOE to establish surrogate models, which can be used to predict the response of other points in the design space with adequate accuracy. Surrogate models have been successfully applied to a variety of optimization cases in recent years. The predictions from surrogate models are usually more efficient than numerical simulations, and the computational cost of optimizations based on surrogate models is usually negligible.
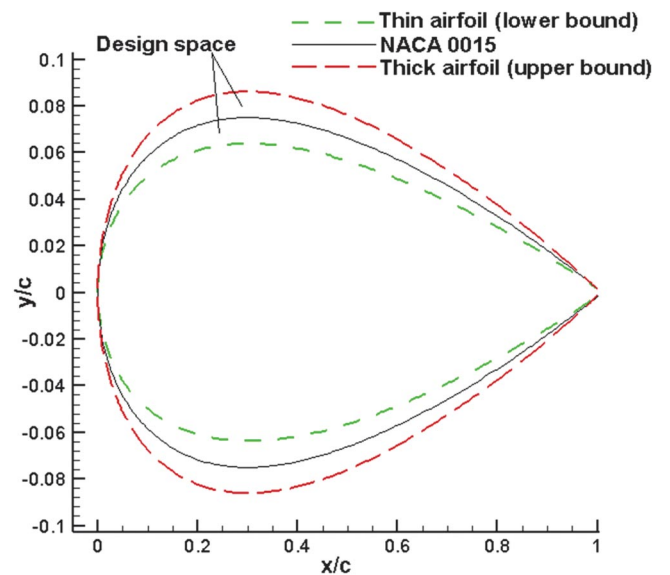

Fig. 7 Schematic of the design space for airfoil optimization in the present study.

Generally, a suitable choice of the surrogate model for a specific problem is in an attempt to get the required accuracy with a least number of sampling points, and a number of surrogate models are present in the literatures. In the present study, the kriging model [27,28] is adopted to construct the approximated model to replace the actual time-consuming CFD solver.

a. Kriging Model. The kriging model is an interpolation approach, which provides predictions with an unknown function, like a "black box." In the kriging model, the response $y(x)$ can be generally written in terms of the sum of a constant μ and a random function $Z(x)$ as follows:

$$y(\boldsymbol{x}) = \boldsymbol{\mu} + Z(\boldsymbol{x}), \qquad \boldsymbol{x} \in R^n \qquad (9)$$

in which $\boldsymbol{\mu}$ is obtained from the information of sampling data. $Z(\cdot)$ denotes a random process with zero mean and variance σ^2, whose covariance is

$$\text{COV}[Z(x^{(i)}), Z(x^{(j)})] = \sigma^2 R(x^{(i)}, x^{(j)}) \qquad (10)$$

in which $R(x^{(i)}, x^{(j)})$ is the correlation function, and just depending on the Euclidean distance between $x^{(i)}$ and $x^{(j)}$ ($i = 1, \ldots, n_s$ and $j = 1, \ldots, n_s$; n_s represents the number of sampling points).

In this paper, the Gaussian exponential correlation function is used, which can be written as

$$R(x^{(i)}, x^{(j)}) = \exp\left(-\sum_{k=1}^{n} \theta_k |x_k^{(i)} - x_k^{(j)}|^{p_k}\right) \qquad (11)$$

in which n represents the number of design variables, $x^{(i)}$ denotes the ith sampling point, and $\boldsymbol{\theta} = [\theta_1, \theta_2, \ldots, \theta_n]$ and $\boldsymbol{P} = [P_1, P_2, \ldots, P_n]$, $(1 < P_k \leq 2)$ are hyper-parameter vectors to be optimized.

The predicted response at any untried x can be written as follows:

$$\tilde{y}(x) = \tilde{\boldsymbol{\mu}} + \boldsymbol{r}^T(x)\boldsymbol{R}^{-1}(y_s - \tilde{\boldsymbol{\mu}}1) \qquad (12)$$

in which $\boldsymbol{y}_s = [y^{(1)}, y^{(2)}, \ldots, y^{(n_s)}]$, and $1 \in R^n$ is a vector filled with ones; r is a correlation matrix between the untried x and sampling points, and $\boldsymbol{R}$ is a correlation vector, and they are defined by

$$\boldsymbol{r}(x) := [R(x^{(i)}, x)]_i \in R^n \qquad (13)$$

$$\boldsymbol{R} := [R(x^{(i)}, x)]_i \in R^n \qquad (14)$$

And $\tilde{\boldsymbol{\mu}}$ is the minimum square estimation of the form

$$\tilde{\boldsymbol{\mu}} = (1^T \boldsymbol{R}^{-1}1)^{-1} 1^T \boldsymbol{R}^{-1} \boldsymbol{y}_s \qquad (15)$$

The mean-square error for the prediction is defined by

$$S^2 = \sigma^2 [1 - \boldsymbol{r}^T \boldsymbol{R}^{-1} \boldsymbol{r} + (1 - \boldsymbol{r}^T \boldsymbol{R}^{-1}1)^2/(1^T \boldsymbol{R}^{-1}1)] \qquad (16)$$

in which σ^2 is the estimation of process variance and defined by

$$\sigma^2 = \frac{1}{n_s}(\boldsymbol{y}_s - 1\tilde{\boldsymbol{\mu}})^T \boldsymbol{R}^{-1}(\boldsymbol{y}_s - 1\tilde{\boldsymbol{\mu}}) \qquad (17)$$

Finally, to solve the vector of hyper-parameters $\boldsymbol{\theta}$ and $\boldsymbol{P}$, a numerical-optimization algorithm is generally used to search the maximum likelihood estimation (MLE) of the following function:

$$\mathrm{MLE}(\boldsymbol{\theta}, \boldsymbol{P}) = -(n_s \ell_n \sigma^2(\boldsymbol{\theta}) + \ln |\boldsymbol{R}(\boldsymbol{\theta})|) \qquad (18)$$

b.   Method of Adding New Sample Points.   Once the kriging model is established making use of the sample data, optimization can be conducted through any algorithm with a low computational cost. However, although the kriging model has a good capability of global approximation, using this method has a great chance to achieve a local optimal point depending on the distribution of initial sampling points, due to the uncertainty of the kriging model [29].

The aforementioned problem can be solved by directly adding new sample data, which are obtained by the expensive numerical simulations. In the present study, to effectively consider both the estimated function values and the uncertainties in the kriging model, the excepted improvement (EI) [30] approach is introduced to add new sampling points in the optimization process.

Assuming $y_{\min}$ is the minimum of the object function among the n_s sample points, and $y(x)$ is a Gaussian distribution function with mean $\tilde{y}(x)$ and variance σ^2, $y(x) \in N\{[(\tilde{y}(x), \sigma^2)]\}$. The improvement at any untried point x can be written as

$$I(x) = y_{\min} - \tilde{y}(x) \qquad (19)$$

And the excepted estimation of $I(x)$ can be written as

$$EI_{(x)} = \begin{cases} \left(y_{\min} - \tilde{y}(x)\right)\Phi\left(\dfrac{y_{\min} - \tilde{y}(x)}{s}\right) + s\phi\left(\dfrac{y_{\min} - \tilde{y}(x)}{s}\right) & (s > 0) \\[2mm] 0 & (s = 0) \end{cases} \qquad (20)$$

in which Φ and ϕ denote the cumulative distribution function and probability density function, respectively.

After finishing each optimization, two new sample points are added at the locations where the EI value is maximum and the objective value is optimum [minimizing the predictor (MP)], respectively, until a convergent optimum is achieved. This method improves the accuracy of the kriging model, and makes a compromise between global and local optimization [29]. In this study, the GA is applied to search for the maximum of EI.

C.   Optimization-Algorithm Method

With regard to the objective functions, the general categories of optimization processes are classified as single-objective optimizations and multi-objective optimizations. For the first category, the process is driven by a single-objective function to search for a single optimal solution, whereas for the second, more than one objective function drive the process to finally achieve tradeoffs between them.

Optimization algorithms, which can be adopted to find an optimal solution or a set of optimal solutions for specific problems in some defined design spaces, have been widely used in many fields. To deal with specific problems, a large number of optimization algorithms are developed based on different numerical methods or logical strategies. Generally, these methods fall into the category of numerical-optimization algorithms or global-optimization algorithms. Numerical-optimization algorithms, such as the method of feasible directions [31] and nonlinear conjugate gradient method [32], are usually much quicker than the intelligent optimization algorithms. However, the results of numerical-optimization algorithms highly rely on the initial value, which may result in a local optimum if the start searching point is given improperly. On the contrary, global-optimization algorithms, which are capable of achieving the global optimum without calculating the local gradient, have no strict requirement of the start searching point. Some of the global-optimization algorithms include simulated annealing [33] algorithms, GAs [34,35], particle-swarm-optimization [36] algorithms, etc.

In this study, the aerodynamic optimization of an airfoil for the cycloidal propeller can be considered as a single-objective-function-optimization problem. And the GA is adopted as the optimization methodology. The main reason of choosing GA is as follows. Unlike traditional numerical-optimization techniques, such as the gradient-based method, a GA works with a population instead of a single point. Besides, the optimal solution searching process of the GA is not based on any gradient information [22]. Therefore, for the unsteady aerodynamic problem of a cycloidal propeller, which has highly nonlinear characteristics associated with discontinuities and multipeak in the design space, GA has a great chance to achieve the global optimal solution.

GAs are search-optimization approaches, which model the principles of natural evolution and generate optimal solutions using the process of natural genetics and natural selections. In an optimization process based on the GA, searching starts with some randomly selected points (initial population). Then, by evaluating the fitness of each individual, a set of individuals that can best adapt to the natural environment is selected in each generation. Being regarded as the potential solutions, these selected individuals are subsequently sent to the next generation with crossover and mutation according to a certain probability. This step is repeated from generation to generation until the optimization convergence criteria are satisfied. The framework of the GA can be clearly summarized as follows:

  1) Initialize the population.

  2) Calculate the fitness of each individual.

  3) Select the individuals to the next generation according to the evaluation of step 2.

  4) Conduct the operation of crossover

  5) Conduct the operation of mutation

  6) Create a subpopulation of next generation.

  7) If the stopping criteria are met, go to step 8; otherwise, go to step 2.

  8) Output the best optimal solution, and stop the optimization.

D.   Methodology of CFD Simulations

During the rotation, all the blades of a cycloidal propeller pitch cyclically; the wake caused by the pitching motion of one blade can significantly affect the flowfields of others, making the interferences among blades strongly unsteady and complex. Therefore, for the aerodynamic-optimization design of an airfoil for cycloidal propellers, it is better to consider all the blades as a whole instead of an individual airfoil.

1.   Numerical Setup

In the process of constructing and refining the surrogate model, sampling data are required by running the expensive unsteady CFD simulations. In this study, the main methodology of 2-D unsteady CFD simulations for cycloidal propellers is based on our previous research [37].

A 2-D incompressible unsteady CFD solver in the commercial software FLUENT 14.0 is adopted to solve the RANS governing equations [38]. Because of the incompressibility of the flow, the pressure-based solver is used, which has a good capability of solving the low-speed incompressible flows. The RANS governing equations are solved implicitly [39], and the SIMPLE algorithm is taken as the pressure–velocity coupling approach. The dual-time method [40] is used for unsteady iterations, and the Green–Gauss node-based method [41] is adopted in gradient interpolation. The pressure implicit with splitting of operators algorithm [42] is applied to make a coupling between the velocity and pressure terms. The convective-flux terms and diffusive-flux terms are discretized with the second-order-accurate upwind scheme [43] and second-order-accurate central-difference scheme [44], respectively.

To describe the pitch motions of blades, one sine function with a mean is adopted to build a simplified mathematical model of the form [37,45]

$$\alpha(\psi) = \left(\frac{\alpha_{\text{top}} + \alpha_{\text{bot}}}{2}\right) \cdot \sin(\psi) + \frac{\alpha_{\text{bot}} - \alpha_{\text{top}}}{2} \tag{21}$$

in which $\alpha(\psi)$ is the blade pitch angle at azimuth ψ, and α_{top} and α_{bot} are the blade pitch angle at the top and bottom positions of the cycloidal cage, respectively. This simplified model has been validated to be capable of well approximated with the actual blade pitch-angle variation in [37,45]. Readers can obtain more details about the numerical setup in [37].

2.   Sliding-Mesh Method

In [37], the dynamic-mesh approach, which combined the spring-based smoothing technique [46] with the local remeshing technique [47], was adopted to deal with the problem of mesh deformation caused by the rigid motion of blade pitching and rotation. Although this method allows a fully general motion of the moving boundaries, the remeshing and updating processes at each time step incur a great increase of computational time [48]. This is more obvious for periodic aerodynamic problems, such as the analysis of unsteady aerodynamics, in which the convergent numerical solutions are usually achieved in several cycles. And it will be particularly significant for the present aerodynamic optimization, which needs a number of numerical simulations to be conducted to construct the surrogate model.

Another moving-mesh method is the sliding-mesh method. In this method, remeshing is avoided by dividing the computational domain into several zones, which move relative to each other along suitably selected boundaries. This method has been widely used in aerodynamic numerical simulations with moving boundaries, both in conjunction with unstructured and structured grids [49,50]. Therefore, in this study, the sliding-mesh technique [51,52] is adopted to model the blade motions in all numerical simulations.

E.   Framework of Optimization Design

The framework of aerodynamic-optimization design of an airfoil for cycloidal propellers is as follows:

1) Choose the initial samples of airfoils based on the OLHD method.

2) Calculate the aerodynamic responses at the sampling points by the CFD solver.

3) Construct the kriging surrogate model.

4) Use GAs to search for the two new points, in which EI is maximum or the objective function is optimum, respectively.

5) Use the CFD solver to calculate the aerodynamic responses of the two points found by step 4.

6) If the convergent criteria are met, go to step 7; otherwise, use the two points to update the samples and go to step 3.

7) Output the optimal airfoil.

The process is illustrated in Fig. 8.

III.   Results and Discussions

A.   Validations of the Numerical-Simulation Method

To validate the numerical-simulation method, two validation cases have been made. One is conducted on an oscillating airfoil with low Reynolds number and low Mach number; the other is conducted on a four-bladed cycloidal propeller in hover, which is the baseline model to be optimized in the present study.

1.   Validation Case 1: Oscillating Airfoil

Simulations on the characteristics of the pitching NACA 0012 airfoil [53] were conducted at $Re = 1.35 \times 10^5$ and $M = 0.0386$ using the numerical method mentioned earlier. The airfoil was oscillated at $k = \omega_p c / 2V_\infty = 0.1$ with $\alpha_p(t) = 10 + 15 \sin(\omega_p t)$, in which k is the oscillating reduced frequency, ω_p is the circular frequency, and t is the time.

The general view of the computational domain and mesh distribution around the airfoil is illustrated in Fig. 9. As shown in Fig. 9a, the whole domain is a rectangle of 40 chords long and 20 chords wide. The computational domain is divided into two parts linked by the mesh interface: one is the outer domain and another is the oscillating airfoil domain. Figure 9b shows the close view of the mesh domain around the oscillating airfoil. The height of the first row
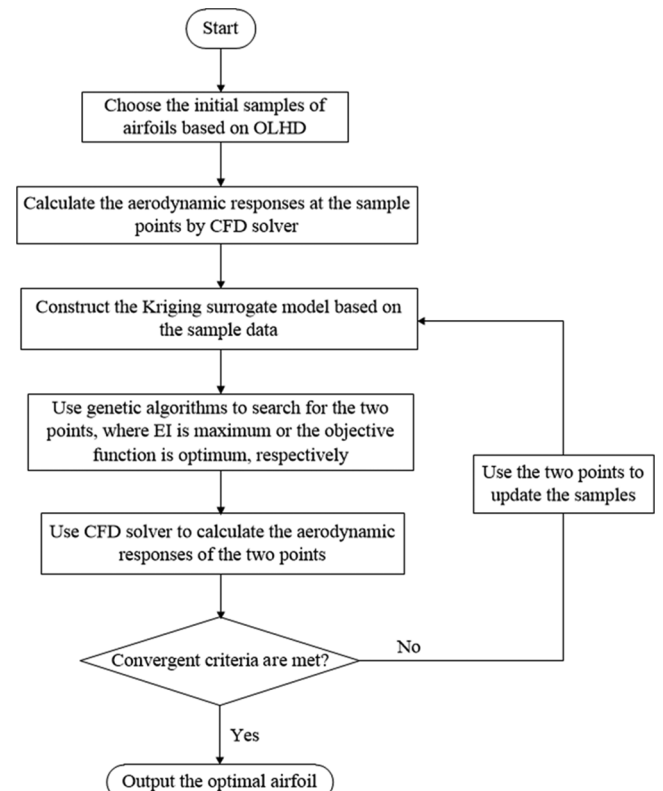

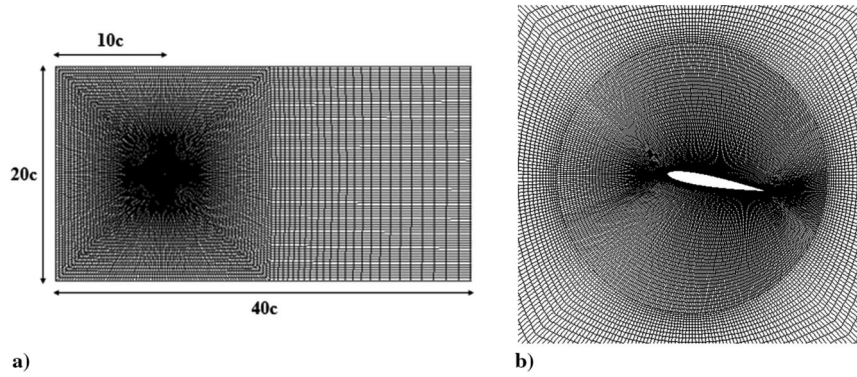Fig. 8   Process of aerodynamic optimization of an airfoil for cycloidal propellers.

Fig. 9   a) The whole computaion domain and b) the mesh around the airfoil.
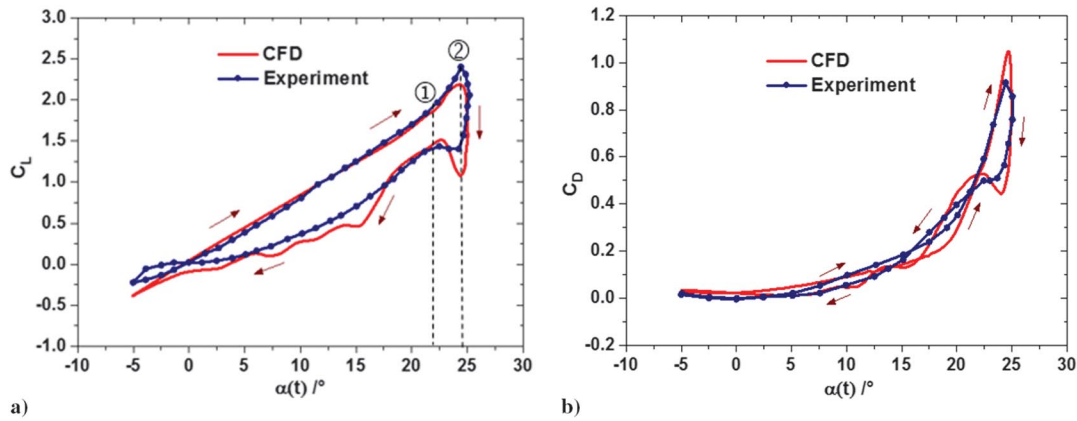

Fig. 10   Comparisons of computational results and experimental data [53]: a) lift-coefficient and b) drag-coefficient.

mesh is set such that the $y+$ is equal to 1 [54]. The mesh-dependency study is made, and the structured grid of 481×51 is finally applied to generate the mesh in the oscillating airfoil domain.

Figure 10 shows the comparisons of computational variations of dynamic aerodynamic loads and experimental data [53] during one oscillation period. As shown in Fig. 10, the computational dynamic lift and drag loops agree well with the experimental data, although some discrepancies exist. In addition, Figs. 11 and 12 show the comparisons of computational flow structures and conceptual sketch experimental flow structure of two typical dynamic events during upstroke, which include the formation (Fig. 11) and catastrophic detachment (Fig. 12) of the leading-edge vortex (LEV). As shown in Figs. 11 and 12, the numerical simulations capture the same flow structures as that obtained by the flow visualizations. (The experimental flow visualization can be seen in [53].) As shown in Fig. 11, when $\alpha_p = 21.9$ deg ↑ (corresponds to the point   in Fig. 10a), the turbulent breakdown rapidly moves upstream and downstream and disrupts the separation bubble, an LEV is formed on the upper surface of the airfoil (see [53]). After that, as the airfoil continues to pitch up, the LEV grew ($\sim$ in Fig. 10a) and convects downstream with an increase of the lift coefficient for $\alpha_p = 21.9 \sim 24.7$ deg. As shown in Fig. 12, at $\alpha_p = 24.7$ deg (corresponds to point in Fig. 10a, near the maximum pitching angle of the airfoil pitching motion), the LEV moves closer to the trailing

edge of the airfoil (about $0.9c$; see [53]) and causes a maximum lift coefficient $C_{L \max}$ (see Fig. 10a), with experimental data of $C_{L \max} = 2.44$ and computational data of $C_{L \max} = 2.28$.

The preceding discussion shows that the present numerical-simulation method is suitable for computing the dynamic aerodynamic responses and flow characteristics of an airfoil under pitching motion at low Reynolds number and low Mach number.

2.   Validation Case 2: Baseline Cycloidal Propeller

The design parameters of the baseline cycloidal-propeller model [12] for optimization in this research are as follows. The cycloidal propeller consists of four blades with NACA 0015, the radius of the cycloidal propeller is $R = 0.076$ m, the span length is $B_L = 0.1715$ m, the chord length is $c = 0.033$ m, the maximum pitching angles at the top and bottom positions of the cycloidal-propeller cage are both 40 deg, and the rotation speeds range from 400 to 1800 rpm.

The definition of coordinate system is shown in Fig. 13a, and the computational domains for simulating the flowfield of a cycloidal propeller are shown in Figs. 13b–13e. The whole mesh is composed of six domains, which include one outer domain, one rotation domain, and four-blade domains. The outer domain is a stationary part with structured meshes, whose boundary extends to as far as 20 times of the rotor diameter to make sure that the wake generated by
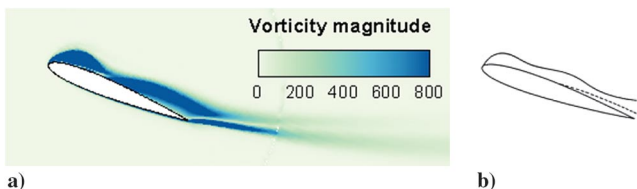

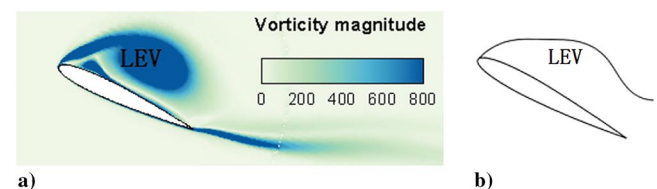**Fig. 11   Comparison of computational and experimental flow structure during the formation of LEV.**

Fig. 12   Comparisons of flow structure for $\alpha_p = 24.7$ deg: a) computational result and b) experiment [53].
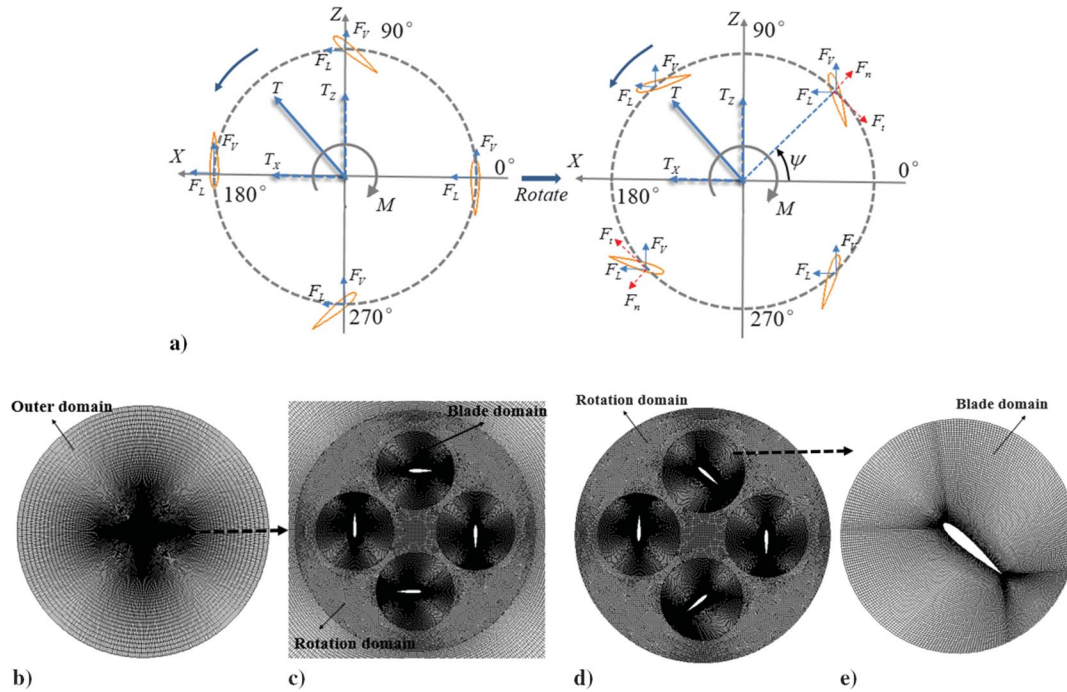
Fig. 13 **a) Coordinate system, b) outer domain, c) initial rotor domain, d) rotor domain after rotating, and e) blade domain.**

the cycloidal propeller dies away. In the rotation domain, the hybrid-mesh method is adopted to generate meshes, whereas in the four-blade domains, structured meshes are generated in conjunction with boundary grids, which aims to reduce the numerical dissipation and capture the flow features near the blade in detail. To pass fluid properties from one side of the domain to another, the overlapping surface between different subdomains is defined as the interface. In addition, the grid-convergence study with different mesh levels is carried out. To ensure both efficiency and accuracy, the mesh number in each blade domain is eventually selected to be 491×57, and the total mesh number of the whole computational domain is about 2.5×10^5.

In this research, two nondimensional coefficients are introduced to describe the aerodynamic performance of 2-D cycloidal propellers, which are defined by

$$C_T = \frac{T}{(1/2)\rho V_R^2 S} \tag{22}$$

$$C_M = \frac{P}{(1/2)\rho V_R^2 \cdot R \cdot \omega \cdot S} = \frac{P}{(1/2)\rho V_R^3 S} \tag{23}$$

in which C_T and C_M are the resultant thrust coefficient and aerodynamic-torque coefficient, respectively. R and ω represent the radius and rotational speed of the cycloidal propeller, respectively. $V_R = R \cdot \omega$ represents the rotation velocity of the blade. $S = D \cdot B_L$ is the projected area of the cycloidal propeller; D and B_L represent the diameter and blade-span length of the cycloidal propeller, respectively.

Figure 14 shows the comparisons of computational aerodynamic results and experimental data [12] under different rotation speeds. Figures 14a and 14b show the resultant thrust coefficients C_T and aerodynamic-torque coefficients C_M, which are calculated by Eqs. (22) and (23) with $V_R = 14.3$ m/s at the rotation speed of 1800 rpm, respectively. It can be clearly seen that the computational results of C_T and C_M agree well with the experimental data. However, at high rotation speeds of 1600 and 1800 rpm, both the predictions of C_T and C_M are underestimated to some extent. For instance, at the rotation speed of 1800 rpm, the experimental C_T and C_M are 0.571 and 0.53, whereas the computational C_T are 0.537 and 0.491, respectively.

The discrepancies have also been found in [2,37,55]. Especially, in [55], the authors have compared both 2-D and 3-D CFD hover results with experiments, and found similar discrepancies (within 15%) at higher rotational speeds. The reasons may be illustrated as follows. Firstly, the measured resultant thrust of the cycloidal-propeller experimental model may be produced not only by the blades of the cycloidal propeller, but also by other rotating parts in the experimental model [2]. Hence, the computational results of the resultant thrust, which are simulated without considering the hub arm and linkages, may be lower than the measured data [37]. Secondly, when the aerodynamic power measurements were acquired, the total power consumed by the whole cycloidal-propeller experimental model was firstly measured, and then tare tests were conducted after removing all the blades to measure the balance losses and profile power associated with the structure of the cycloidal propeller (i.e., hub arm and linkages); these measurements were then subtracted from the total power to obtain the aerodynamic power required to rotate the blades. However, the aerodynamic power measured by this method may not be the pure aerodynamic power for a cycloidal propeller with only blades, because when the cycloidal propeller was rotating, the interference between its structure and the blades may have affected the flow around the blades, and thus caused an induced aerodynamic power to some extent. Therefore, although the structures were removed, some additional effects probably cannot be considered. This may be the reason why the aerodynamic torque is underestimated in the numerical simulations.

As shown in Fig. 14c, in spite of the slight underestimation of the C_T and C_M at high rotation speeds of 1600 and 1800 rpm, the computational C_T–C_M ratios correlate very well with the experimental data under different rotation speeds.

Overall, the preceding validations and discussions show that the computational method and mesh setup are suitable for simulating the aerodynamics and flows of the oscillating airfoil and the 2-D cycloidal propeller. Therefore, in the following sections, the same scheme is employed in the optimization of airfoils for a cycloidal propeller.

B. Objective and Constraints

As mentioned earlier, all blades of the cycloidal propeller are simulated as a whole in the present study. As a result, those commonly used objective functions of aerodynamic-optimization
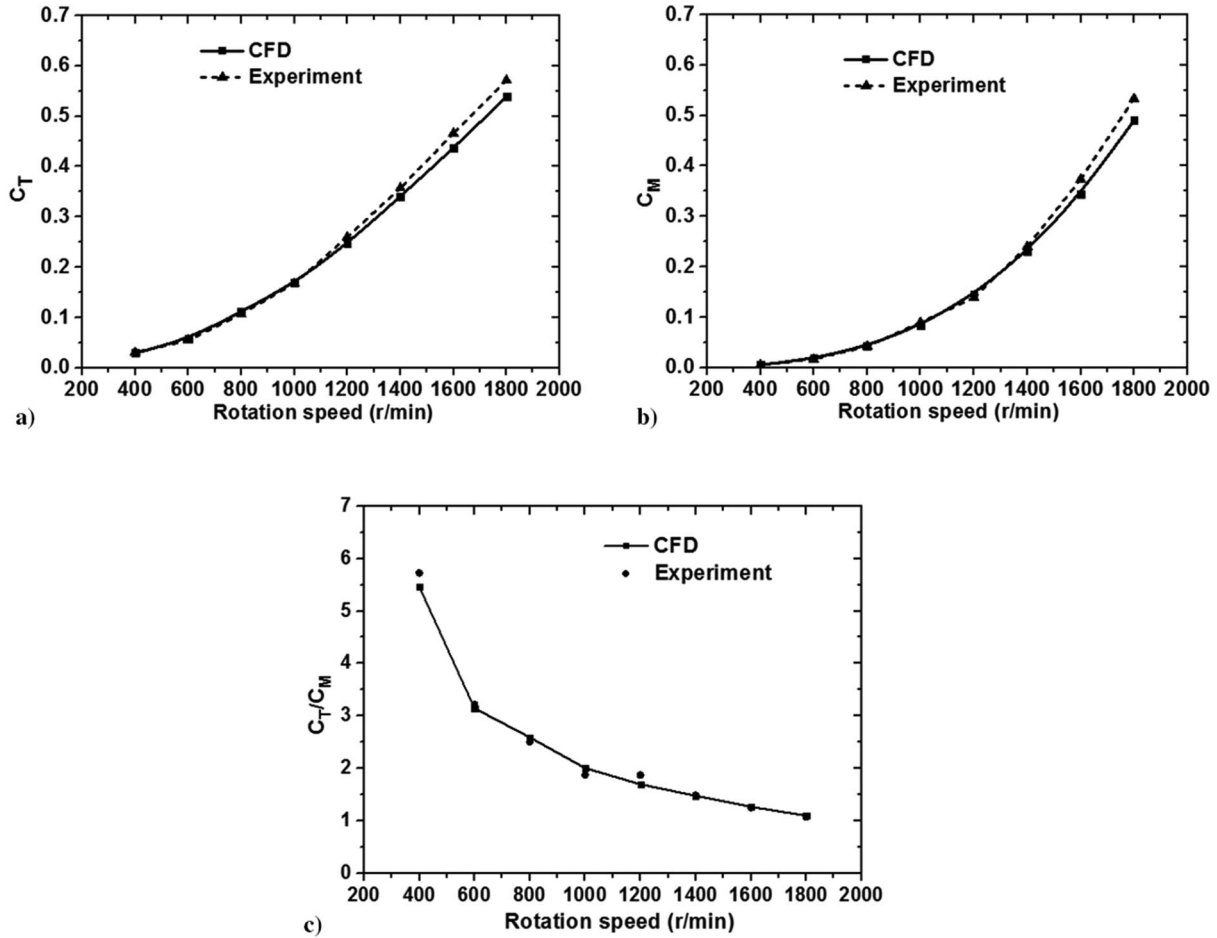
Fig. 14   Comparisons of computational results and experimental data [12]: a) CT, b) CM, and c) CT/CM.

design for a single airfoil, such as the lift–drag ratio, may not be suitable to that of a cycloidal propeller.

For a cycloidal propeller in hover, the FM can be used to estimate its overall aerodynamic performance [1], which is defined by

$$FM = \frac{PL\sqrt{DL}}{\sqrt{2\rho}} \tag{24}$$

$$PL = \frac{T}{P} \tag{25}$$

$$DL = \frac{T}{S} \tag{26}$$

in which ρ represents the air density, and PL and DL represent the power loading and disk loading, respectively. Generally, a higher FM indicates that a better aerodynamic performance of the cycloidal propeller is achieved in hover. Substituting Eqs. (22) and (23), and (25) and (26) into Eq. (24), the FM can be written as follows:

$$FM = \frac{C_T}{C_M \cdot V_R} \cdot \frac{\sqrt{0.5\rho V_R^2 \cdot C_T}}{\sqrt{2\rho}} = \frac{1}{2} \cdot \frac{C_T^{1.5}}{C_M} \tag{27}$$

According to Eq. (27), the objective of the optimization in the present study is to maximize the term $(1/2 \cdot C_T^{1.5}/C_M)$, or minimize the term $(-1/2 \cdot C_T^{1.5}/C_M)$. The mathematical model can be described as follows:

$$\begin{cases} \text{minimize :} & -\frac{1}{2} \cdot \frac{C_T^{1.5}}{C_M} \\ \text{subject to} & (1) C_T \geq C_{T0} \\ & (2) C_M \leq C_{M0} \\ & (3) |\Delta\zeta_{max}| - 0.15 \cdot \zeta_{max} \leq 0 \end{cases} \tag{28}$$

in which C_{T0} and C_{M0} are the baseline resultant thrust coefficient and aerodynamic-torque coefficient, respectively; ζ_{max} is the maximum thickness of the baseline airfoil.

C.   Optimization Results and Discussion

For the kriging-based optimizer, a set of 81 initial sample points has been generated by the OLHD method. The EI and MP methods are simultaneously used; the kriging surrogate models are refined repetitively by adding the new sample data at each iteration. Finally, 15 iterations are finally conducted and 111 sample points are acquired to construct the kriging model. In each case, the initial GA population size is held constant to be 150, and the crossover rate and mutation rate are 0.8 and 0.02, respectively. The iterations of the GA optimization terminate until the stop criteria meet; for instance, the function-evaluation budgets exceed some specified value.

The optimization convergence histories of the resultant thrust coefficient C_T, aerodynamic-torque coefficient C_M, and FM are shown in Fig. 15. As shown in Fig. 15, the optimization is convergent about 70 generations. Table 1 shows the comparison of optimization results and that of the baseline model. As shown in Table 1, compared with the baseline model, the optimized resultant thrust coefficient C_T is increased by 4.6% (from 0.5391 to 0.5639) and the optimized aerodynamic-torque coefficient C_M is decreased by −9.58% (from 0.4905 to 0.4435). And the FM is increased by 18.31% (from 0.4035 to 0.4774).
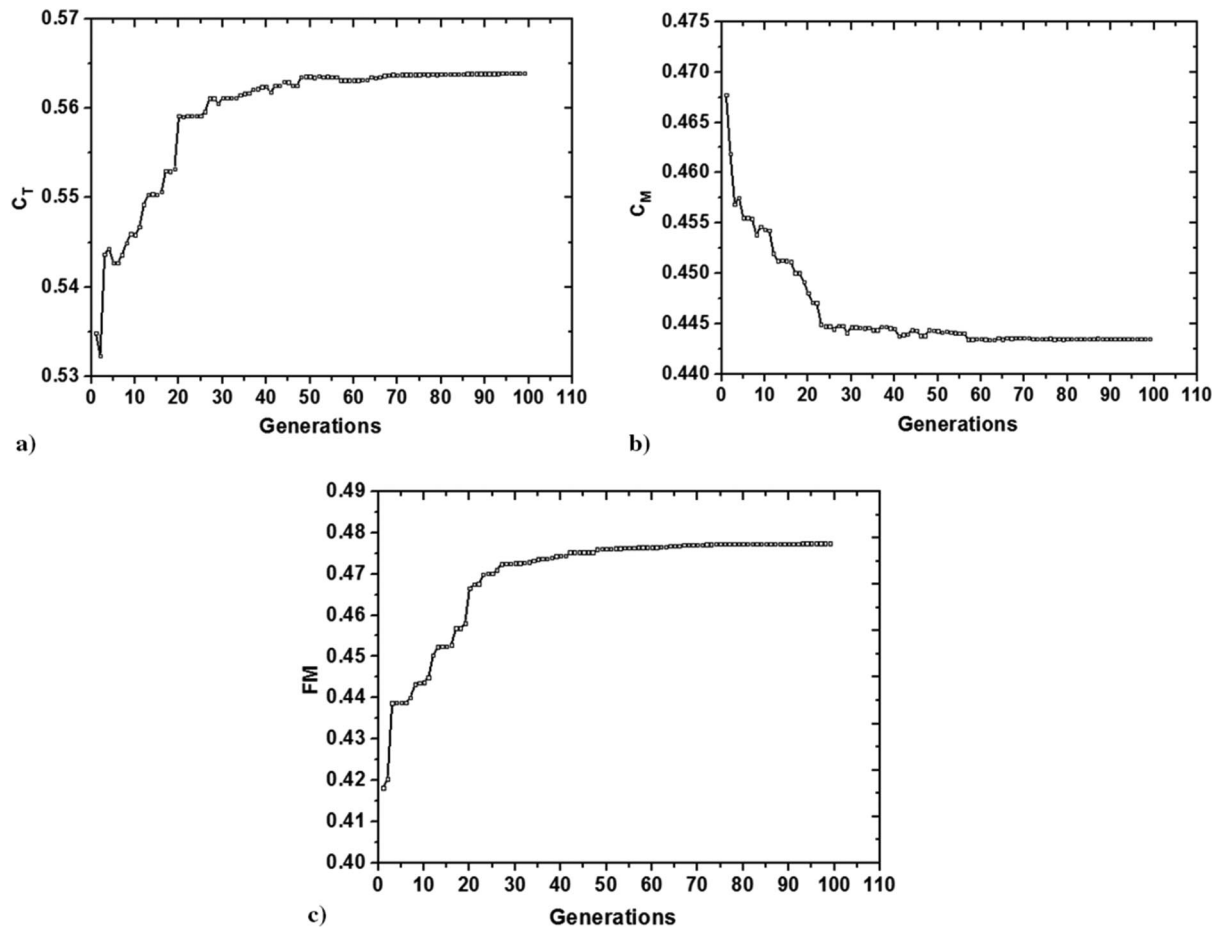
Fig. 15   Optimization convergence histories of a) C_T, b) C_M, and c) FM.

Figure 16 shows the comparisons of aerodynamic performance (C_T, C_M, FM) between the cycloidal propeller with an optimized airfoil and the cycloidal propeller with NACA 0015 airfoil, for a rotation speed range of $400 \sim 1800$ rpm. As shown in Figs. 16a and 16b, compared with the baseline model, C_T and C_M curves are relatively higher and lower, respectively. And the comparison presented in Fig. 16c shows that the FM apparently improves in the wide range of rotation speed.

Figure 17 shows the comparison of geometries of the optimized airfoil and baseline (NACA 0015). From Fig. 17, it can be clearly seen that the maximum thickness of the optimized airfoil is higher than the baseline airfoil (NACA 0015), but lower than the airfoil specified by the upper boundary in the design space. To some extent, this is consistent with the conclusions drawn from the experiments [12,19]. In [12], in which the baseline model in this study is selected, the experiments showed that the cycloidal propeller with the NACA 0015 airfoil achieved the highest hovering aerodynamic efficiency, followed by the NACA 0010 airfoil and the NACA 0006 airfoil. In [19], comparisons of test cases of an airfo0il with plate, NACA 0006, NACA 0012, NACA 0015, and NACA 0018 showed that the cycloidal propeller with the NACA 0015 airfoil had the highest FM. This behavior may be illustrated as follows. For the airfoil of plate, NACA 0006, NACA 0010, NACA 0012, and NACA 0015, both the averaged lift (mainly contributes to the thrust) and drag (mainly contributes to the aerodynamic torque) during one oscillation period probably become higher with the increase of thickness, but compared

with the drag, the lift affects the lift–drag ratio (or FM) more significantly, which leads to the highest FM for the cycloidal propeller with the NACA 0015 airfoil, as shown in [12,19]. However, when the thickness of the airfoil continues to increase, the drag increase begins to play a more significant role in the change of FM. Therefore, when the thickness of the airfoil finally increases to a certain value (the thickness is about $16.2\%c$, in which FM reaches its maximum for the present case) FM begins to decrease. As a result, the cycloidal propeller with the NACA 0018 airfoil in [19] showed lower FM than that with the NACA 0015 airfoil. And it also may be the reason why the thickness of the optimum airfoil is higher than NACA 0015, but lower than the airfoil specified by the upper boundary in the design space.

In addition, it is very interesting to see from Fig. 17 that the optimum airfoil has a small amount of positive camber (about 0.5%). Most of the previous researches on cycloidal propellers mainly focused on the symmetric airfoil, because the camber is intuitively not an obvious choice for a cycloidal propeller, considering the blade sections will operate at both positive and negative pitching angles during its rotation [1]. Therefore, the blade with a positive camber will have a negative camber during the lower half of the cage. However, the optimization results in this study show that an airfoil with a small amount of camber may be a better choice for the cycloidal propeller. This discovery is consistent with the experiments on conventional rotors at low Reynolds numbers, which showed that a small amount of blade camber can significantly improve the aerodynamic performance of the rotor system [56].

Generally, the increased maximum thickness and camber may cause greater suction (higher lift) on the upper surface of the airfoil, but, meanwhile, with an increased pressure gradient causing laminar separation, hence higher drag [57–59]. And, as stated previously, the airfoil with a positive camber will have a negative camber during the lower half of the cycloidal-propeller cage. These tradeoffs suggest searching the optimum airfoil thickness and camber for a specific

Table 1   Optimization results at the design point (1800 rpm)

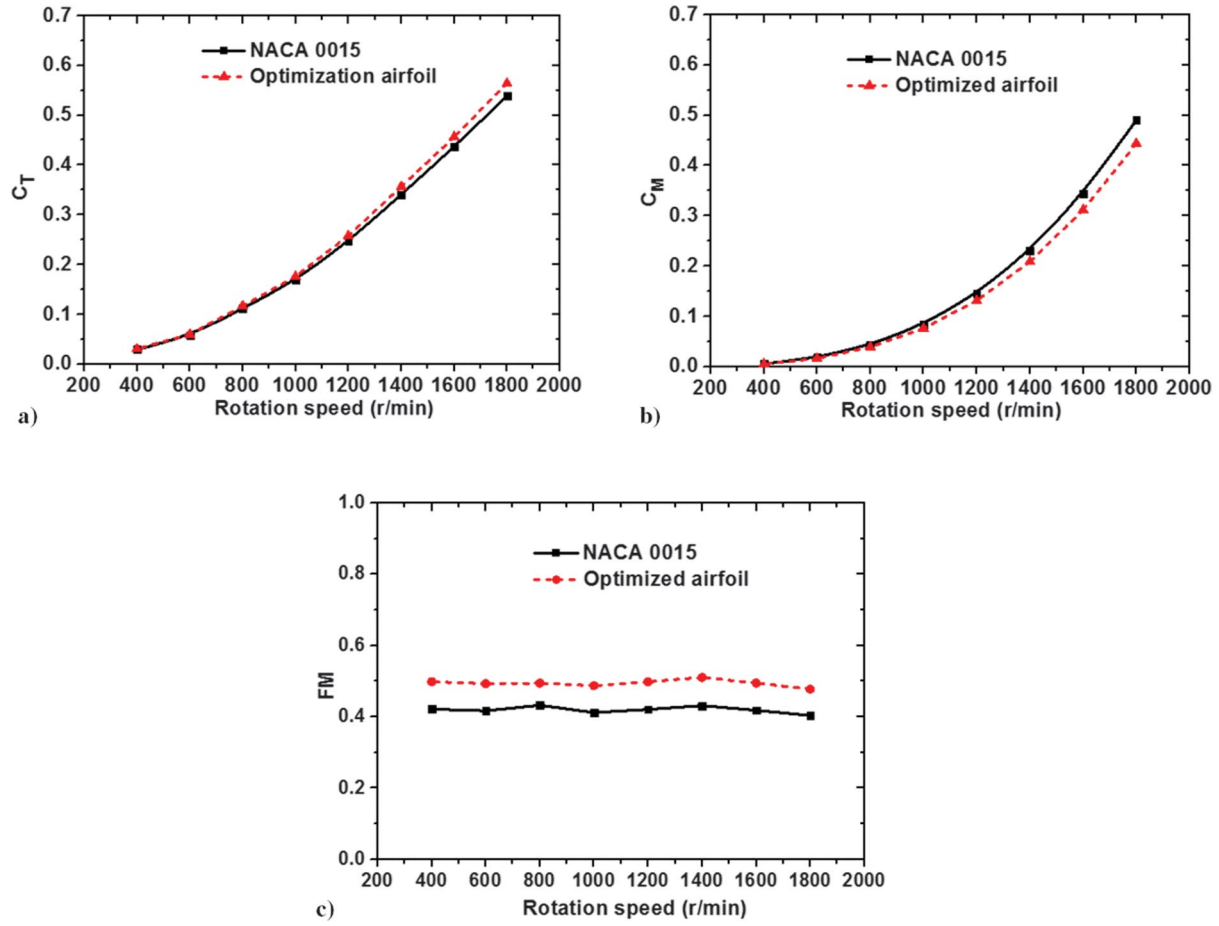|	C_T	C_M	FM $= 0.5C_T^{1.5}/C_M$	Runs of flow solver
Baseline	0.5391	0.4905	0.4035	— —
Optimization	0.5639	0.4435	0.4774	111
$\Delta/\%$	+4.6	−9.58	18.31	— —

Fig. 16　Comparisons of the aerodynamic performance of cycloidal propellers a) C_T, b) C_M, and c) FM.
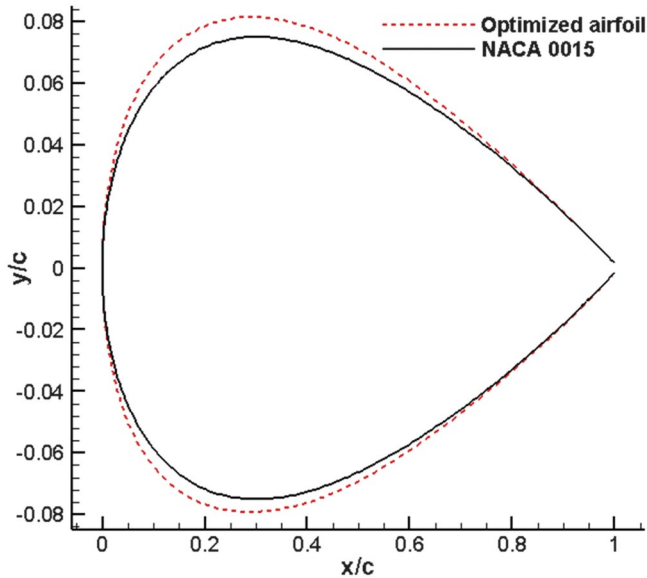

Fig. 17　Comparison of geometries of optimized airfoil and the baseline (NACA 0015).

case (i.e., the Reynolds number and pitching amplitude of the airfoil) through an optimization approach. When it comes to the present case, compared with the symmetric airfoil, the optimized airfoil with a small amount of camber achieves better aerodynamic performance, probably owing to suffering from less performance degradation due to the laminar separation, which results in relatively higher time-averaged lift with lower time-averaged drag penalty. However, it is worth noting that, as both the thickness and camber of the optimized

airfoil are different from the baseline airfoil in the present case, further detailed parametric studies and verifications on how the thickness or camber of the airfoil individually affects the cycloidal-propeller performance need to be conducted in the future.

The comparisons of the instantaneous blade aerodynamic variations between the optimized airfoil and NACA 0015 (baseline) are shown in Fig. 18. And Fig. 19 shows the comparisons of the instantaneous rotor aerodynamic variations between the optimized cycloidal propeller and the baseline. The blade vertical-force coefficient C_{VF}, blade lateral-force coefficient C_{LF}, and blade aerodynamic-torque coefficient C_{mb} shown in Fig. 18 are defined by

$$C_{VF}(\psi) = \frac{F_V(\psi)}{(1/2)\rho V_R^2 B_L c} \qquad (29)$$

$$C_{LF}(\psi) = \frac{F_L(\psi)}{(1/2)\rho V_R^2 B_L c} \qquad (30)$$

$$C_{mb}(\psi) = \frac{M_b(\psi)}{(1/2)\rho V_R^3 B_L c} \qquad (31)$$

in which F_V and F_L represent the instantaneous blade vertical force and blade lateral force, respectively. The vertical-thrust coefficient C_{VT} and lateral-thrust coefficient C_{LT} shown in Fig. 19 are defined by

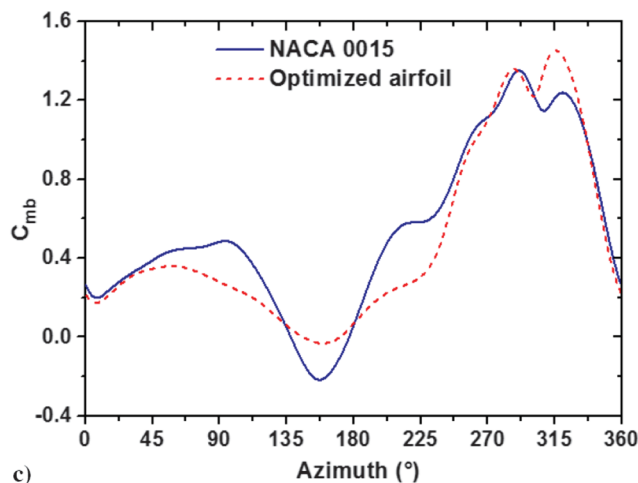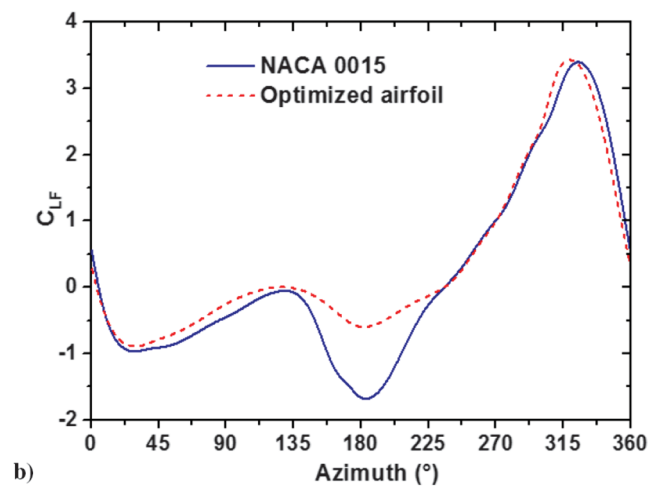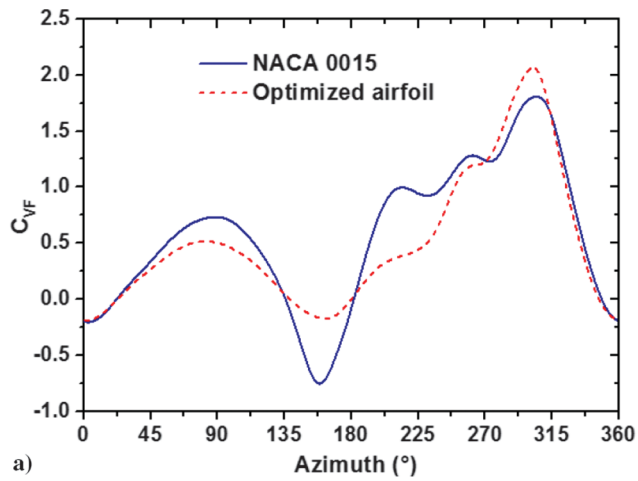$$C_{VT}(\psi) = \frac{T_V(\psi)}{(1/2)\rho V_R^2 B_L D} \qquad (32)$$

Fig. 18   Comparisons of blade aerodynamic variations with azimuth:
a) C_{VF}, b) C_{LF}, and c) C_{mb}.

Fig. 19   Comparisons of rotor aerodynamic variations with azimuth:
a) C_{VT}, b) C_{LT}, and c) C_M.

$$C_{LT}(\psi) = \frac{T_L(\psi)}{\frac{1}{2}\rho V_R^2 B_L D} \tag{33}$$

in which T_V and T_L represent the instantaneous vertical-thrust component and lateral-thrust component, respectively.

As shown in Fig. 18a, for the blade vertical-force-coefficient variations with azimuth, the major difference between the optimized airfoil and the baseline lies in the interval of $45 \sim 245$ deg. Although the negative C_{VF} in the azimuths of $135 \sim 180$ deg is higher than that of the NACA 0015 airfoil, the positive C_{VF} of the optimized airfoil in
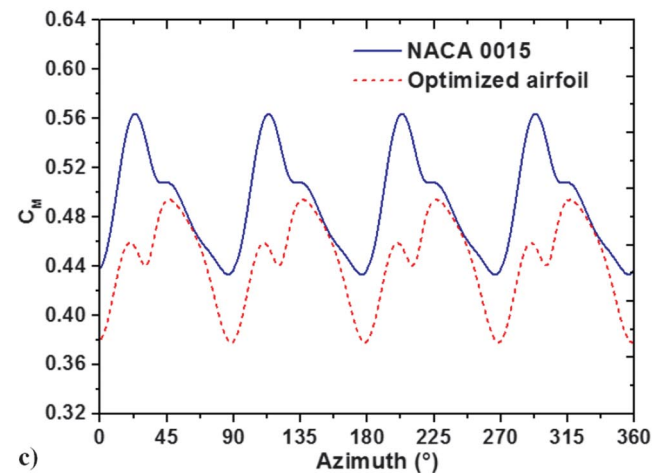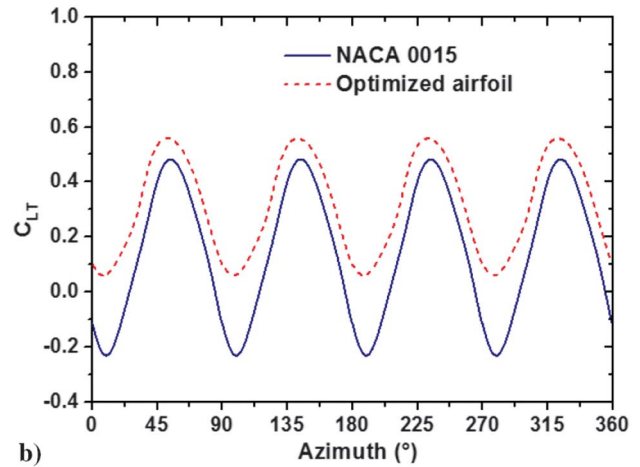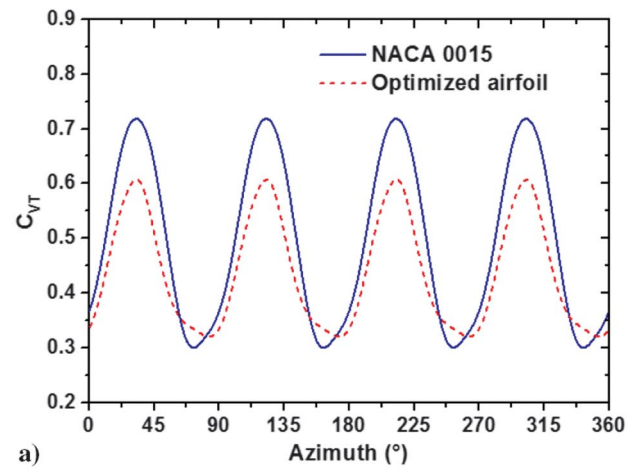
the azimuths of $45 \sim 135$ and $180 \sim 245$ deg is clearly lower than that of NACA 0015. Therefore, as shown in Fig. 19a, both the peak of variations of C_{VT} and the corresponding azimuth-averaged value are lower than that of the NACA 0015 airfoil.

As shown in Fig. 18b, for the lateral blade-force variations of both airfoils, the negative C_{LF} mainly lies in the interval of $0 \sim 180$ deg, whereas the positive C_{LF} mainly lies in the interval of $180 \sim 360$ deg. The major difference of C_{LF} between the two airfoils lies in the interval of $135 \sim 225$ deg, in which the negative C_{LF} of the optimized airfoil is much higher than that of NACA 0015. As a result, the lateral-thrust coefficient C_{LT} of the cycloidal propeller

with the NACA 0015 airfoil varies both in the positive and negative regions, whereas C_{LT} of the cycloidal propeller with the optimized airfoil varies only in the positive region, which leads to a much higher positive azimuth-averaged lateral thrust in one cycle (Fig. 19b). Therefore, although the vertical thrust is lower, the resultant thrust of the cycloidal propeller with the optimized airfoil is still higher than the baseline, owing to its much higher lateral thrust.

As shown in Fig. 18c, for the blade torque-coefficient variations during one revolution, the major difference between the two airfoils lies in the interval of $45 \sim 245$ and $300 \sim 330$ deg. The C_{mb} of the optimized airfoil is higher than that of the baseline in azimuths of $135 \sim 180$ and $300 \sim 330$ deg, whereas it is clearly much lower than that of the baseline in azimuths of $45 \sim 135$ and $180 \sim 245$ deg. Therefore, as shown in Fig. 19c, the aerodynamic-torque-coefficient variations show that the azimuth-averaged C_M achieves a lower value for the cycloidal propeller with the optimized airfoil than that with the NACA 0015 airfoil.

For an oscillating airfoil, the unsteady aerodynamic force can be illustrated by plotting the instantaneous lift and drag against the pitching angles. However, as the relative flow velocities experienced by the blade keep changing in both magnitudes and directions during rotation, the analysis of the unsteady aerodynamics of the cycloidal-propeller blade is much more complicated. An alternative is to plot the blade normal-force coefficients C_N and tangent-force coefficients C_t vs blade pitching angles [37], as shown in Fig. 20.

In Fig. 20, C_N and C_t are defined by

$$C_N(\psi) = \frac{F_n(\psi)}{(1/2)\rho V_R^2 B_L c} \tag{34}$$

$$C_t(\psi) = \frac{F_t(\psi)}{(1/2)\rho V_R^2 B_L c} \tag{35}$$

in which Ψ represents the azimuth of the blade, and the blade normal force F_n and tangent force F_t are defined by

$$F_n(\psi) = F_V(\psi) \cdot \sin(\psi) - F_L(\psi) \cdot \cos(\psi) \tag{36}$$

$$F_i(\psi) = F_V(\psi) \cdot \cos(\psi) - F_L(\psi) \cdot \sin(\psi) \tag{37}$$

As shown in Fig. 20, the blade-force curves of the optimized airfoil and NACA 0015 are in similar pattern, and both the blade normal-force and tangent-force curves are clearly hysteresis loops, showing the strong effect of an unsteady effect. It is worth noting that, in Fig. 20, the negative C_N means that the direction of the blade force points from the blade to the center of the cycloidal-propeller cage. For the blade force, the difference of force curves between the optimized airfoil and NACA 0015 mainly lies in pitching angles of $40 \downarrow \sim -40$ deg $\downarrow$ during downstroke (left cycle of the cycloidal-propeller cage).

To further illustrate the difference of unsteady blade force between the optimized airfoil and NACA 0015 (Fig. 20), the instantaneous pressure contours and streamlines of the blade at different azimuths in one cycle are shown in Fig. 21.

As shown in Fig. 21, when $\psi = 0$ deg $\uparrow$ ($\alpha_p = 0$ deg $\uparrow$), the separated LEVs at the trailing edge can be seen on the lower surface of both airfoils, and the pressure contours and streamlines for the cases of the two airfoils are almost the same, except that the time of the separated LEVs is slightly delayed. Thus, C_N for the case of the optimized airfoil is slightly higher at the instant (Fig. 20a). When $\psi = 22.5$ deg, $\alpha_p = 15.3$ deg $\uparrow$, the trailing-edge vortices (TEVs) appear on both airfoils, with little difference in both C_N and C_t. When $\psi = 45 \sim 67.5$ deg, $\alpha_p = 28.3 \sim 37$ deg $\uparrow$, the streamlines around two airfoils are almost the same, but a relatively lower pressure is observed at the leading edge of the upper surface of the NACA 0015 airfoil, which results in a higher C_N than that of the optimized airfoil. When the airfoil moves to the upmost location of the cycloidal-propeller cage ($\psi = 90$ deg, $\alpha_p = 40$ deg $\uparrow$), where the downwash of the cycloidal propeller has less influence on the airfoil, the streamlines are highly curved due to the significant inverse camber effect [19]. As shown in Figs. 21a and 21b, the inverse camber effect increases the AOA of the airfoil at the leading edge and causes an LEV, which increases the C_N and C_t. And the LEV is relatively larger for the case of the NACA 0015 airfoil, resulting in higher C_N and C_t. After that, the airfoil begins to pitch down (downstroke). When $\psi = 90 \sim 135$ deg ($\alpha_p = 40, 28.3$ deg $\downarrow$), the LEV moves from the leading edge to the trailing edge on the upper surface of both NACA 0015 and the optimized airfoil. However, as the LEV of NACA 0015 remains more energetic than that of the optimized airfoil, C_N and C_t are relatively higher for the case of NACA 0015. When $\psi = 135 \sim 180$ deg ($\alpha_p = 28.3, 0$ deg $\downarrow$), C_N of both airfoils are negative, and compared with NACA 0015, C_N of the optimized airfoil is relatively higher. When $\psi = 157.5 \sim 180$ deg ($\alpha_p = 15.3, 0$ deg $\downarrow$), the LEVs clearly disappear for both airfoils, and a relatively much lower negative pressure is observed on the lower surface of NACA 0015, which contributes to a lower negative C_N at the instant. When $\psi = 180 \sim 247.5$ deg ($\alpha_p = 0, -37$ deg $\downarrow$), the pressure on the lower surface of NACA 0015 remains lower. As a result, C_N of NACA 0015 remains lower and C_t of NACA 0015 remains higher than that of the optimized airfoil. When the airfoil is located at the bottom of the rotor cage ($\psi = 270$ deg), the pitching angle is -40 deg; however, because there is downwash in the rotor cage and downwash induced by the LEV shedding from the upper stream blade, the AOA of both airfoils are relatively small and not stalled. The streamlines and pressure distribution for both airfoils are almost the same and result in little difference in both C_N and C_t at the instant. When $\psi = 292.5$ deg ($\alpha_p = -37$ deg $\uparrow$), leading-edge separation bubbles (LESBs) can be observed on the lower surface of both airfoils. When $\psi = 315$ deg ($\alpha_p = -28.5$ deg $\uparrow$), the LESBs develop into LEVs for both airfoils. Although the pitching angle is decreasing, the TEV shed from the upstream airfoil induces the upwash and increases
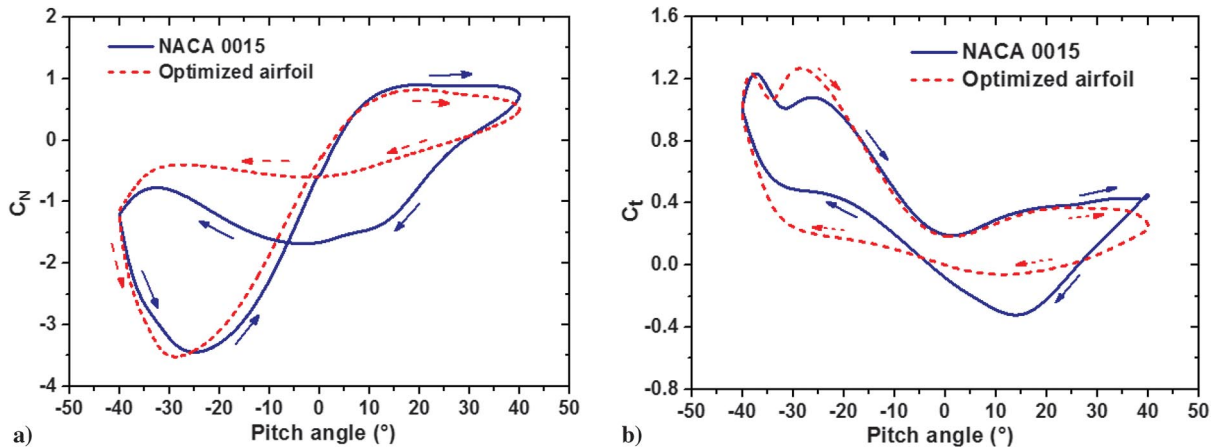

Fig. 20 Comparisons of blade-force coefficients: a) C_N and b) C_t.
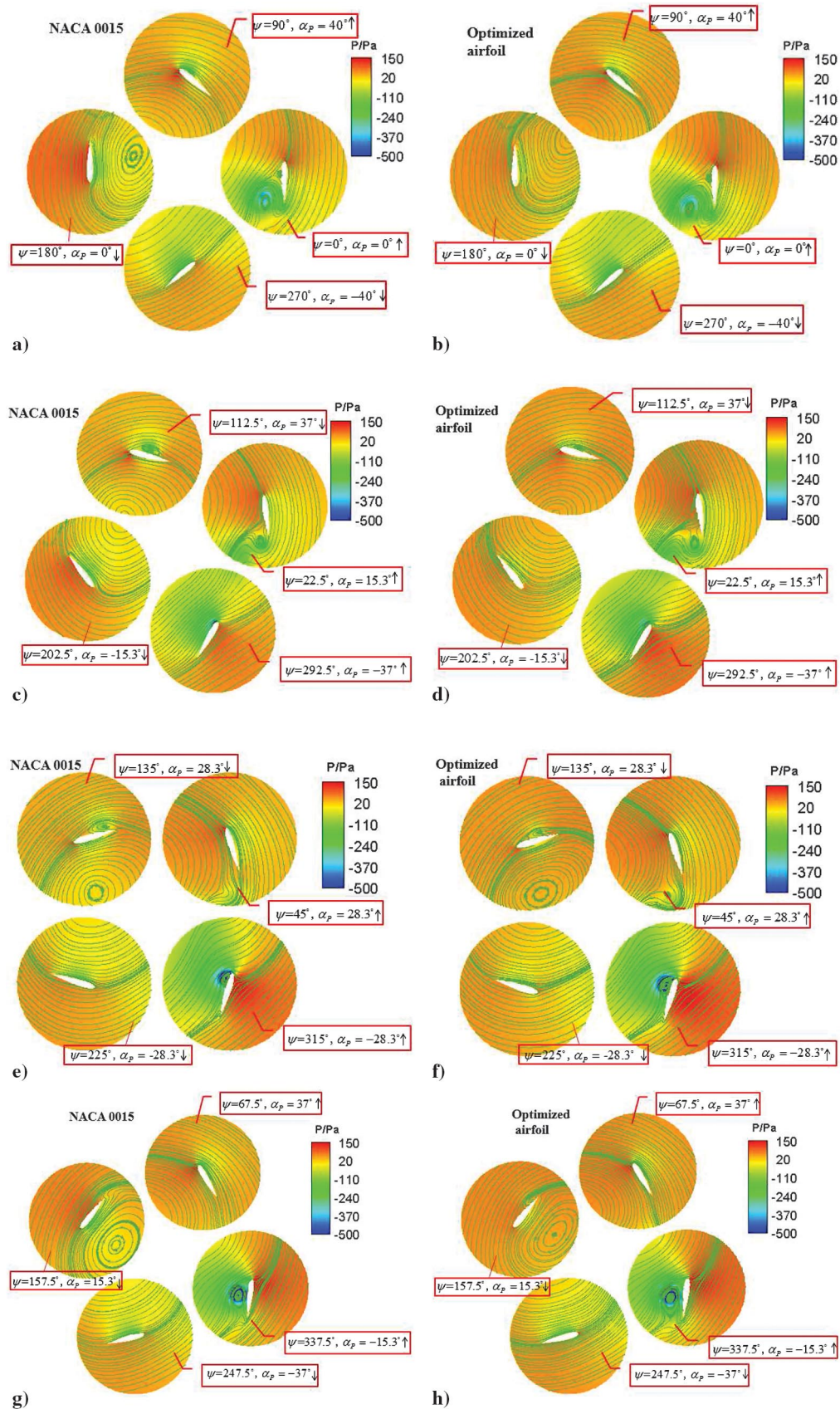
Fig. 21   Comparisons of pressure contours and streamlines: a, c, e, g) NACA 0015 and b, d, f, h) optimized airfoil.

the AOA, and force peaks of C_N appear at the instant. But, for the case of NACA 0015, the LEV is delayed, and hence the corresponding C_N peak appears later. After that, the LEVs move from the leading edge to the trailing edge, and then downstream,

and the upwash induced by the shedding TEV from the upstream airfoil becomes weaker, decreasing the induced AOA and C_N. Here, again, due to the delay of the LEV, there is an azimuth lag for the C_N curve of the NACA 0015 airfoil.

IV.   Conclusions

An aerodynamic-optimization-design method of an airfoil for cycloidal propellers in hover is established. The CST geometry representation method is used to define the airfoil shape with different geometrical parameters. The sample data in the design space are selected using the OLHD methodology. The actual aerodynamic performance of cycloidal propellers is simulated by using the time-dependent incompressible RANS CFD method and the sliding-mesh technique, which are verified by validation cases on the oscillating NACA 0012 airfoil and the baseline cycloidal-propeller model. Using the sample data, surrogate models are constructed based on the kriging model. During simulations, all blades of the cycloidal propeller are simulated as a whole, and the FM are selected to be the objective functions. To determine the optimized airfoil in the design space, the GA is adopted on the basis of the kriging model.

The results show that the maximum thickness of the optimized airfoil is higher than the baseline airfoil (NACA 0015), but lower than the airfoil specified by the upper boundary in the design space. Besides, the optimized airfoil has a small amount of positive camber, which indicates that an airfoil with a suitable amount of positive camber may be a better choice than the symmetric airfoil for cycloidal propellers.

The FM of the cycloidal propeller at the design point (1800 rpm) increases by about 18.31% from 0.4035 of the baseline airfoil (NACA 0015) to 0.4774 of the optimized airfoil, with the resultant thrust coefficient rising by 4.6% and the aerodynamic torque falling by 9.58%. In addition, although the optimization is conducted only at the design rotation speed, an appreciable improvement of the FM is achieved for a wide range of rotation speeds.

Furthermore, according to the aerodynamic characteristic analysis on thrust variations with azimuth in one cycle, the time-averaged vertical-thrust component of the cycloidal propeller with the optimized airfoil is lower than that with the baseline airfoil, but the corresponding time-averaged lateral thrust is much higher than the baseline cycloidal propeller. The flowfield variations with azimuth and the unsteady blade-force variations with pitching angles show that the difference in blade force and flowfield mainly lies in the azimuths of $90 \sim 270$ deg during the blade downstroke (left cycle of the cycloidal-propeller cage).

Acknowledgments

References

[1] Benedict, M., Ramasamy, M., and Chorpra, I., "Performance of a Cycloidal Rotor Concept for Micro Air Vehicle Applications," *Journal of the American Helicopter Society*, Vol. 55, No. 2, 2010, Paper 22002.
doi:10.4050/JAHS.55.022002

[2] Iosilevskii, G., and Levy, Y., "Experimental and Numerical Study of Cyclogiro Aerodynamics," *AIAA Journal*, Vol. 44, No. 12, 2006, pp. 2866–2870.
doi:10.2514/1.8227

[3] Hwang, I. S., and Kim, S. J., "Aerodynamic Performance Enhancement of Cycloidal Rotor According to Blade Pivot Point Movement and Preset Angle Adjustment," *KSAS International Journal*, Vol. 9, No. 2, 2008, pp. 58–63.

[4] Siegel, S., Seidel, J., and Cohen, K., "A Cycloidal Propeller Using Dynamic Lift," *37th AIAA Fluid Dynamics Conference and Exhibit*, AIAA Paper 2007-4232, June 2007.

[5] Hwang, I. S., Min, S. Y., and Lee, C. H., "Development of a Four-Rotor Cyclocopter," *Journal of Aircraft*, Vol. 45, No. 6, 2008, pp. 2151–2157.
doi:10.2514/1.35575

[6] Hu, Y., Kim, L., and Hu, W. R., "The Research on the Performance of Cyclogyro," *6th AIAA Aviation Technology, Integration and Operations Conference (ATIO)*, AIAA Paper 2006-7704, Sept. 2006.

[7] Fagley, C., Porter, C., and McLaughlin, T., "Curvature Effects of a Cycloidally Rotating Airfoil," *52nd Aerospace Sciences Meeting*, AIAA Paper 2014-0255, Jan. 2014.

[8] Wheatley, J. B., and Windler, R., "Wind-Tunnel Tests of a Cyclogiro Rotor," NACA TN 528, 1935.

[9] Kirsten, F. K., "Cycloidal Propulsion Applied to Aircraft," *Transactions of the American Society of Mechanical Engineers*, Vol. 50, No. AER-50-12, 1928, pp. 25–47.

[10] Benedict, M., Chopra, I., Ramasamy, M., and Leishman, L. G., "Experimental Investigation of the Cycloidal-Rotor Concept for a Hovering Micro Air Vehicle," *Proceedings of AHS International 64th Annual Forum*, American Helicopter Soc., Alexandria, VA, 2008, pp. 1071–1092.

[11] Benedict, M., Ramasamy, M., Chopra, I., and Leishman, L. G., "Experiments on the Optimization of the MAV-Scale Cycloidal Rotor Characteristics Towards Improving Their Aerodynamic Performance," *Proceedings of International Specialists Meeting on Unmanned Rotorcraft 2009*, American Helicopter Soc., Alexandria, VA, Jan. 2009, pp. 410–429.

[12] Jarugumilli, T., Benedict, M., and Chopra, I., "Experimental Optimization and Performance Analysis of a MAV Scale Cycloidal Rotor," *49th AIAA Aerospace Sciences Meeting Including the New Horizons Forum and Aerospace Exposition*, AIAA Paper 2011-821, Jan. 2011.

[13] Sirohi, J., Parsons, E., and Chopra, I., "Hover Performance of a Cycloidal Rotor for a Micro Air Vehicle," *Journal of the American Helicopter Society*, Vol. 52, No. 3, 2007, pp. 263–279.
doi:10.4050/JAHS.52.263

[14] Kim, S., Chul, Y. Y., Daesung, K., Youngha, Y., and Illkyung, P., "Design and Performance Tests of Cycloidal Propulsion Systems," *44th AIAA/ASME/ASCE/AHS Structures, Structural Dynamics, and Materials Conference*, AIAA Paper 2003-1786, April 2003.

[15] Hwang, I. S., Hwang, C. S., Min, S. Y., Jeong, I. O., Lee, C. H., Lee, Y. H., and Kim, S. J., "Design and Testing of VTOL UAV Cyclocopter with 4 Rotors," *Proceedings of AHS International 62nd Annual Forum*, American Helicopter Soc., Alexandria, VA, 2006, pp. 2100–2106.

[16] Zachary, H. A., and Casey, F., "Novel Cyclorotor Pitching Mechanism for Operation at Curtate and Prolate Advance Ratios," *51st AIAA Aerospace Sciences Meeting Including the New Horizons Forum and Aerospace Exposition*, AIAA Paper 2013-0501, Jan. 2013.

[17] Nozaki, H., Sekiguchi, Y., and Matsuuchi, K., "Research and Development on Cycloidal Propellers for Airships," *18th AIAA Lighter-Than-Air Systems Technology Conference*, AIAA Paper 2009-2850, May 2009.

[18] Matsuuchi, K., Ohtsuka, N., and Kimura, Y., "Cycloidal Propeller and Its Application to Advanced LTA Vehicles," *AIAA's 3rd Annual Aviation Technology, Integration, and Operations (ATIO)*, AIAA Paper 2003-683, Nov. 2003.

[19] Hu, Y., and Zhang, H. L., "An Investigation into the Effect of the Airfoil on the Aerodynamics of the MAV Scale Cycloidal Propeller Under Hovering Status," *15th AIAA/ISSMO Multidisciplinary Analysis and Optimization Conference*, AIAA Paper 2014-3015, June 2014.

[20] Kulfan, B. M., and Bussoletti, J. E., "'Fundamental' Parametric Geometry Representations for Aircraft Component Shapes," *11th AIAA/ISSMO Multidisciplinary Analysis and Optimization Conference*, AIAA Paper 2006-6948, Sept. 2006.

[21] Kulfan, B. M., "A Universal Parametric Geometry Representation Method–'CST'," *45th AIAA Aerospace Sciences Meeting and Exhibit*, AIAA Paper 2007-62, Jan. 2007.

[22] Antunes, A. P., and Azevedo, J. L. F., "Studies in Aerodynamic Optimization Based on Genetic Algorithms," *Journal of Aircraft*, Vol. 51, No. 3, 2014, pp. 1002–1012.
doi:10.2514/1.C032095

[23] Sacks, J., Welch, W. J., Mitchell, T. J., and Wynn, H. P., "Design and Analysis of Computer Experiments," *Statistical Science*, Vol. 4, No. 4, 1989, pp. 409–423.
doi:10.1214/ss/1177012413

[24] McKay, M. D., Beckman, R. J., and Conover, W. J., "A Comparison of Three Methods for Selecting Values of Input Variables in the Analysis of Output from a Computer Code," *Technometrics*, Vol. 21, No. 2, 1979, pp. 239–245.

[25] Park, J. S., "Optimal Latin-Hypercube Designs for Computer Experiments," *Journal of Statistical Planning and Inference*, Vol. 39, No. 1, 1994, pp. 95–111.
doi:10.1016/0378-3758(94)90115-5

[26] Shewry, M., and Wynn, H., "Maximum Entropy Design," *Journal of Applied Statistics*, Vol. 14, No. 2, 1987, pp. 165–170.
doi:10.1080/02664768700000020

[27] Krige, D. G., "A Statistical Approach to Some Basic Mine Valuation Problems on the Witwatersrand," *Journal of the Chemical, Metallurgical and Mining Engineering Society of South Africa*, Vol. 52, No. 6, 1951, pp. 119–139.

[28] Matheron, G. M., "Principles of Geostatistics," *Economic Geology*, Vol. 58, No. 8, 1963, pp. 1246–1266.
doi:10.2113/gsecongeo.58.8.1246

[29] Yamazaki, W., Rumpfkeil, M. P., and Mavriplis, D. J., "Design Optimization Utilizing Gradient/Hessian Enhanced Surrogate Model," *28th AIAA Applied Aerodynamics Conference*, AIAA Paper 2010-4363, June–July 2010.

[30] Jones, D. R., Schonlau, M., and Welch, W. J., "Efficient Global Optimization of Expensive Black-Box Functions," *Journal of Global Optimization*, Vol. 13, No. 4, Dec. 1998, pp. 455–492.

[31] Belegundu, A. D., Berke, L., and Patnaik, S. N., "An Optimization Algorithm Based on the Method of Feasible Directions," *Structural Optimization*, Vol. 9, No. 2, 1995, pp. 83–88.
doi:10.1007/BF01758824

[32] Hager, W. W., and Zhang, H. C., "A New Conjugate Gradient Method with Guaranteed Descent and an Efficient Line Search," *SIAM Journal on Optimization*, Vol. 16, No. 1, 2005, pp. 170–192.
doi:10.1137/030601880

[33] Kirkpatrick, S., Gelatt, C. D., and Vecchi, M. P., "Optimization by Simulated Annealing," *Science*, Vol. 220, No. 4598, 1983, pp. 671–680.
doi:10.1126/science.220.4598.671

[34] Deb, K., *Multi-Objective Optimization Using Evolutionary Algorithms*, Wiley, New York, 2003, pp. 7–21.

[35] Goldberg, D. E., *Genetic Algorithms in Search, Optimization and Machine Learning*, Addison Wesley, New York, 1989, pp. 1–18.

[36] Bai, Q. H., "Analysis of Particle Swarm Optimization Algorithm," *Computer and Information Science*, Vol. 3, No. 1, 2010, pp. 180–184.
10.5539/cis.v3n1p180

[37] Tang, J. W., Hu, Y., and Song, B. F., "Investigation on the Unsteady Aerodynamics of Cycloidal Propeller in Hovering Flight," *Journal of Aerospace Engineering*, Vol. 229, No. 13, Nov. 2015, pp. 2519–2536, http://pig.sagepub.com/content/early/2015/04/20/0954410015580652.full.pdf+html.
doi:10.1177/0954410015580652

[38] Wang, S. Y., , Derek, B. I., and Ma, L.et al., "Numerical Investigations on Dynamic Stall of Low Reynolds Number Flow Around Oscillating Airfoils," *Computers and Fluids*, Vol. 39, No. 9, 2010, pp. 1529–1541.
doi:10.1016/j.compfluid.2010.05.004

[39] Yang, Y., Li, D., and Zhang, Z. H., "Influences of Flapping Wing Micro Aerial Vehicle Unsteady Motion on Horizontal Tail," *Acta Aeronautica et Astronautica Sinica*, Vol. 33, No. 10, 2012, pp. 1827–1833.

[40] Jameson, A., "An Assessment of Dual-Time Stepping, Time Spectral and Artificial Compressibility Based Numerical Algorithms for Unsteady Flow with Applications to Flapping Wings," *19th AIAA Computational Fluid Dynamics Conference*, AIAA Paper 2009-4273, June 2009.

[41] Shima, E., Kitamura, K., and Haga, T., "Green–Gauss/Weighted-Least-Squares Hybrid Gradient Reconstruction for Arbitrary Polyhedra Unstructured Grids," *AIAA Journal*, Vol. 51, No. 11, 2013, pp. 2740–2747.
doi:10.2514/1.J052095

[42] Bressloff, N. W., "A Parallel Pressure Implicit Splitting of Operators Algorithm Applied to Flows at All Speeds," *International Journal for Numerical Methods in Fluids*, Vol. 36, No. 5, 2001, pp. 497–518.
doi:10.1002/(ISSN)1097-0363

[43] Warming, R. F., and Beam, R. M., "Upwind Second-Order Difference Schemes and Applications in Aerodynamic Flows," *AIAA Journal*, Vol. 14, No. 9, 1976, pp. 1241–1249.
doi:10.2514/3.61457

[44] Shyy, W., Thakur, S., and Wright, J., "Second-Order Upwind and Central Difference Schemes for Recirculating Flow Computation," *AIAA Journal*, Vol. 30, No. 4, 1992, pp. 923–932.
doi:10.2514/3.11010

[45] McNabb, M. L., "Development of a Cycloidal Propulsion Computer Model and Comparison with Experiment," M.S. Dissertation, Aerospace Engineering Dept., Mississippi State Univ., Mississippi State, MS, 2001.

[46] Yang, Y. X., Hu, C. B., Cai, T. M., and Sun, D. C., "Instantaneous Regression Rate Computation of Hybrid Rocket Motor Based on Fluid–Solid Coupling Technique," *43rd AIAA/ASME/SAE/ASEE Joint Propulsion Conference and Exhibit*, AIAA Paper 2007-5350, July 2007.

[47] Spentzos, A., Barakos, G., Badcock, K., Richards, B. E., Wernert, P., Schreck, S., and Raffel, M., "Investigation of Three-Dimensional Dynamic Stall Using Computational Fluid Dynamics," *AIAA Journal*, Vol. 43, No. 5, 2005, pp. 1023–1033.
doi:10.2514/1.8830

[48] Mathur, S. R., "Unsteady Flow Simulations Using Unstructured Sliding Meshes," *25th AIAA Fluid Dynamics Conference*, AIAA Paper 1994-2333, June 1994.

[49] Durrani, N., Hameed, H., Rahman, H., and Chaudhry, S., "A Detailed Aerodynamic Design and Analysis of a 2D Vertical Axis Wind Turbine Using Sliding Mesh in CFD," *49th AIAA Aerospace Sciences Meeting Including the New Horizons Forum and Aerospace Exposition*, AIAA Paper 2011-541, Jan. 2011.

[50] Rai, M. M., "Navier–Stokes Simulations of Rotor–Stator Interaction Using Patched and Overlaid Grids," *Journal of Propulsion and Power*, Vol. 3, No. 5, 1987, pp. 387–396.
doi:10.2514/3.23003

[51] Filippone, A., "Simulation of Rotating Cylinder with Sliding Meshes," *43rd AIAA Aerospace Sciences Meeting and Exhibit*, AIAA Paper 2005-1409, Jan. 2005.

[52] Hwang, I. S., Min, S. Y., Lee, C. H., and Kim, S. J., "Experimental Investigation of VTOL UAV Cycloidal Propeller Four Rotors," *48th AIAA/ASME/ASCE/AHS/ASC Structures, Structural Dynamics, and Materials Conference*, AIAA Paper 2007-2247, April 2007.

[53] Lee, T., and Gerontakos, P., "Investigation of Flow over an Oscillating Airfoil," *Journal of Fluid Mechanics*, Vol. 512, No. 512, Aug. 2004, pp. 313–341.
doi:10.1017/S0022112004009851

[54] Nobile, R., Vahdati, M., Barlow, J., and Crook, A. M., "Dynamic Stall for a Vertical Axis Turbine in a Two-Dimensional Study," *World Renewable Energy Congress-Sweden, Linköping Electronic Conference Proceedings*, May 2011, pp. 4225–4232.

[55] Yang, K., Lakshminarayan, V. K., and Baeder, J. D., "Simulation of a Cycloidal Rotor System Using an Overset RANS Solver," *Proceedings of the 66th Forum of the American Helicopter Society*, American Helicopter Soc., Alexandria, VA, May 2010, pp. 750–769.

[56] Hein, B., and Chopra, I., "Hover Performance of a Micro Air Vehicle: Rotors at Low Reynolds Number," *Journal of the American Helicopter Society*, Vol. 52, No. 3, 2007, pp. 254–262.
doi:10.4050/JAHS.52.254

[57] Reid, M. R., and Kozak, J., "Thin/Cambered/Reflexed Airfoil Development for Micro Air Vehicle Applications at Reynolds Numbers of 60000 to 100000," *AIAA Atmospheric Flight Mechanics Conference and Exhibit*, AIAA Paper 2006-6508, Aug. 2006.

[58] Biber, K., "Some Examples of Airfoil Design for Future Unmanned Air Vehicle Concepts," *42nd AIAA Aerospace Sciences Meeting and Exhibit*, AIAA Paper 2004-1050, Jan. 2004.

[59] Liebeck, R. H., "Laminar Separation Bubbles and Airfoil Design at Low Reynolds Numbers," AIAA Paper 1992-2735, June 1992.